DESIGN AND DEVELOPMENT OF COMPACT 2-AXIS ACCELEROMETER FOR PANTOGRAPH-CATENARY SYSTEM

YU YAOKANG

MPhil

The Hong Kong Polytechnique University

2024

The Hong Kong Polytechnique University

Department of Electrical and Electronic Engineering

Design and Development of Compact 2-Axis Accelerometer for Pantograph-Catenary System

YU Yaokang

A thesis submitted in partial fulfillment of the requirements for the degree of Master of Philosophy

June 2023

CERTIFICATE OF ORIGINALITY

I hereby declare that this thesis is my own work and that, to the best of my knowledge and belief, it reproduces no material previously published or written, nor material that has been accepted for the award of any other degree or diploma, except where due acknowledgement has been made in the text.

_____ (Signed)

YU Yaokang (Name of Student)

Abstract

Designing a miniature 2-axis accelerometer is attractive for pantograph-catenary interaction system monitoring because the size and weight of sensor adversely affect the dynamic property of the pantograph. The features of fiber Bragg grating along with the femtosecond laser-based inscription technology can be utilized to make not only compact but also robust accelerometer. Therefore, this thesis focuses on designing and fabrication of a compact cantilever based two-axis accelerometer using multicore fiber (MCF) inscribed with FBG by femtosecond laser-based point by point technique. Prior to the fabrication, the stress distribution along the length and cross section of the cantilever beam structure has been evaluated using FEM based software (COMSOL Multiphysics). Furthermore, the frequency response of the cantilever structure with different length has also been investigated. The simulation results have been validated by inscribing an FBG in one of the cores of a homemade three core fiber and subsequently analyzing the frequency response as well as the response to applied acceleration along one axis. Thereafter, a two-axis accelerometer based on a commercial multi core fiber has been fabricated. The two cores of the MCF have been inscribed with well distinguished FBG using femtosecond laser-based point-by-point technique without removing the polymeric coating thereby enhancing the mechanical stability. The sensor has been packaged in a box with a total weight of 5.2 grams. The response of the packaged sensor has been studied by evaluating its performance to applied acceleration up to 5g without damping oil, and up to 25 g with the filling of the box with damping oil.

Acknowledgement

First and foremost, I would like to express my sincerest gratitude to my supervisor, Prof. Hwa-Yaw Tam, for his guidance and consistent support throughout my M.Phil. study. His encouragement helped me pass through many hurdles throughout my research work and it has been a great honor to work under his supervision.

I would like to express my sincere respect to Prof. Chao Lu for his support during the research work.

I would also like to express my gratitude to Dr. Jitendra Narayan Dash, for his continuous help and collaboration that have helped me in many ways during the whole research study. I am indebted to my group members Dr. JingXian Cui, Dr. Xin Cheng, Dr. Dinusha Serandi Gunawardena, Mr. Chern Yang Leong and Mr. Linyue Lu for their invaluable help and support in the laboratory.

I gratefully acknowledge all the other colleagues from the Photonics Research Center and staffs from the Department of Electrical Engineering.

Finally, I would like to express my gratitude to my beloved family for their unconditional love and support.

Contents

Chapter 1. Introduction

1.1 Background and Motivation

In recent years, the importance of railway systems has been increasing due to the rapid development of greener forms of transportation. The installation of railway lines in many cities clearly indicates the global demand and growth potential [1-2]. Electrified trains are powered by overhead lines referred to as a catenary system where a pantograph mounted on the roof of the train is used to collect power through contact with the overhead lines. The pantograph and the catenary combinedly form a dynamically coupled system where both influence each other. The quality of power collection which in turn is affected by the interaction of the pantograph-catenary system. Therefore, the contact force between the pantograph and catenary needs to be monitored for smooth operation of railways [3]. While a high contact force between the catenary wire and the pantograph may damage or wear out the catenary wire prematurely, a low contact force may lead to sparking and arcing between the pantograph and the contact wire [4]. In addition, when a moving pantograph passes through the nodes of the catenary wire, the induced elastic waves would in turn result in an undesirable vibration of the pantograph. The inevitable vibration results in dynamic power coupling between the pantograph and catenary, as well as an unstable contact force. Hence, contact force measurements are of crucial significance to the health of the pantograph-catenary system.

Several types of electronic and fiber-optic sensors have been proposed for pantograph contact force measurements over the past few years. However, because of the high voltage environment, conventional electronic sensors are not suitable for this purpose and can be replaced with optical sensors benefiting from their intrinsic features such as lightweight, compact size and immunity to electromagnetic interference. Optical sensors, on the other hand, benefiting from their intrinsic

features such as immunity to EMI and non-electrical conductivity, are ideal candidates. Optical image processing techniques together with line sensor cameras, optical fiber-based interferometers and fiber Bragg grating (FBG) based sensors have been utilized to measure the contact force [5-8]. Koyama et.al have demonstrated a force sensor based on displacement of marker on the pan-head of pantograph [5]. However, it should be noted that the maintenance of the system can be costly due to the use of lighting devices and line sensor cameras with the performance of the sensor prone to be affected by the weather. Boffi et.al. have proposed a static and a dynamic strain sensor for pantograph-catenary contact force measurements based on Michelson's interferometer [6]. An FBG-based sensor has been proposed for pantograph strain measurement with temperature compensation based on digital filter [9]. In this case, local heating by sunlight or high electric current can cause deformation in the strip that has been used to install the FBG in the pantograph [10]. Furthermore, an S-shaped FBG-based load cell has also been incorporated in pantograph contact force measurements [11]. Moreover, an FBG-based sensing system comprising fiber optic force sensors and accelerometers have been used to monitor the forces between the collector and the overhead power line [12]. Nevertheless, in these scenarios, heavy transducers are needed to be incorporated with the FBG.

In addition, the inertia from the contact strip movements has to be considered and it can be measured in terms of acceleration via the equation $F=ma$ where a refers to the acceleration of the pantograph where the accelerometer was attached, and m is mainly determined by the mass of the current collector of the pantograph. For example, an FBG based sensor has been used to monitor the contact force and acceleration of an underground pantograph-catenary system [13]. Although, a wide range of FBG-based accelerometers are commercially available for one-axis

acceleration measurements, due to the forward and zig zag motions of the pantographs, simultaneous detection of acceleration along the longitudinal and lateral directions are needed [14]. This could be achieved by assembling two one-axis accelerometers. Incorporation of increased number of sensors may lead to a bulky pantograph-catenary system which would deteriorate the dynamic property of the pantograph. Therefore, a lightweight two-axis accelerometer with the capability of measuring acceleration in multiple directions would be a prudent approach for compact and robust measurements.

In this thesis, a detailed numerical investigation of a cantilever beam-based accelerometer is carried out using FEM based simulation technique followed by experimental validation. The cantilever consists of an optical fiber with a small mass attached at its tip and the simulation involves the investigation of stress distribution along the cross section as well as length of the optical fiber. Furthermore, the frequency response of the sensor for different beam lengths is also studied. The simulation results are validated by fabricating a one-axis accelerometer based on a three-core fiber. Thereafter, a two-axis accelerometer based on a commercial multicore fiber was designed and developed. Two of the seven cores of the multi core fiber are inscribed with well distinguished FBGs through the coating using femtosecond laser-based point by point technique and the geometrical position of the FBG as well as the length of the cantilever beam are fixed as per the simulation results. The sensor is fixed inside an aluminum box filled with damping oil and the response of the sensor to applied acceleration up to 25g is investigated to corroborate its robustness.

1.2 Research Objective

The research objective of this study can be summarized as follows:

- To analyze the stress distribution and frequency response of cantilever beam structure using FEM based simulation for the design of two-axis accelerometer.
- To optimize the parameters such as beam length and position of FBG for maximum response of the sensor to applied acceleration.
- To validate the simulation results using a one axis accelerometer based on a homemade three-core fiber.
- To design a lightweight and miniature FBG-based two-axis fiber optic accelerometer for pantograph-catenary system.
- To inscribe the FBGs at optimal positions in two of the seven cores of multicore fiber as per the simulation model.
- The optimized mass at the tip of sensor and beam length for desired resonant frequency.
- To fix the fiber-based accelerometer in a small box to make the whole system compact.
- To study the response of the sensor to applied acceleration in different orientations with and without the filling of box with damping oil.
- To test the robustness of packaged sensor with high acceleration (> 20 g).

1.3 Thesis Outline

This thesis consists of five chapters and the summary of each chapter is as follows.

Chapter 1 presents the introduction that includes the brief overview of pantograph-catenary system and sensors for contact force measurement, the motivation for the project, research objective and the outline of the thesis.

Chapter 2 provides detailed literature reviews for pantograph-catenary system that includes the basic structure and model of the system. This is followed by literature reviews of on inscription of fiber Bragg gratings using UV laser-based phase mask technique as well as femtosecond laser-based point by point and line by line technique. Thereafter, a brief overview of the theory of FBGs is discussed.

Chapter 3 presents the FEM based simulation analysis for the design of cantilever beam-based accelerometer. The stress distribution and frequency response of the cantilever beam for different mechanical parameters are investigated. The simulation results are validated experimentally by designing a one axis accelerometer using a three-core fiber.

Chapter 4 presents the design of a compact and robust 2-axis accelerometer based on seven-core fiber. The inscription of FBGs using femtosecond laser-based point-by-point as well as the fixing of the sensor in a compact box for maximum response are described in detail. The response of the sensor to applied acceleration is investigated with and without damping oil.

Chapter 5 summarizes the current results of the thesis and discusses the potential works that can be done in future.

1.4 List of Publications

1. **Yaokang Yu**, Jitendra Narayan Dash, Jingxian Cui, Dinusha Serandi Gunawardena and Hwa-Yaw Tam, “Miniature Two-Axis Accelerometer Based on Multicore Fiber for Pantograph-Catenary System,” IEEE Transactions on Instrumentation and Measurement, Vol.73, 7005208, 13 July 2023

Chapter 2. Background Review

2.1 Pantograph-catenary interaction

In the railway system, the catenary wires together with the pantograph constitutes the power collection system where the current from the catenary wire gets collected by the train via the pantograph. This leads to a mechanical interaction between pantograph and catenary system that in turn affects the operation of train.

Primarily, a combined system comprising of a mast, message wire, dropper, contact wire, registration arm and cantilever constitute the catenary as shown in Figure 1. As can be seen from the figure, the mast and the bracket hold the other components of the catenary system at a fixed position that allows pantograph to collect electric power. The messenger wire maintains the position of contact wire intact at a fixed position while the copper contact wire provides power to the pantograph through direct electrical contact. The messenger wire is connected to the copper wire by means of a vertical dropper that helps in decentralized transfer of the admissible load on the contact wire. On the other hand, the horizontal force on the contact wire is taken care of by the registration arm [15].

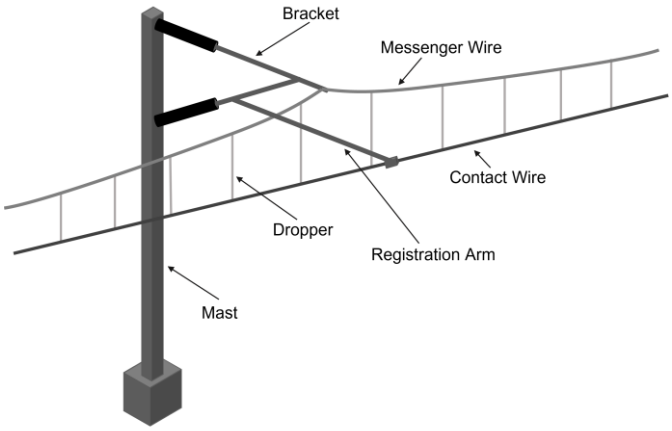

Figure 1. Basic structure of catenary

The pantograph consists of several mechanical components and is mounted on the roof of train for current collection as shown in Figure 2. The pan head remains in contact with the catenary wire for current collection while the other components provide support and uplift force to the pantograph [15,16].

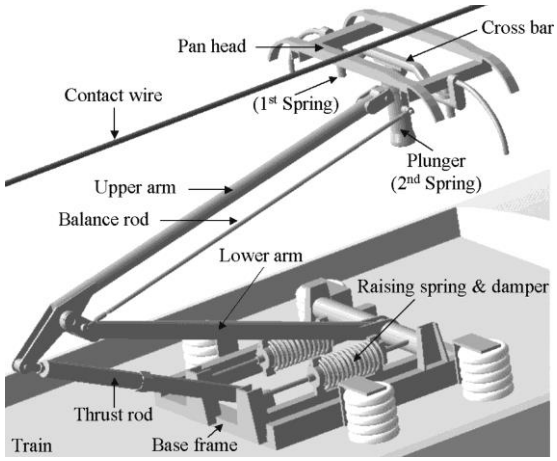

Figure 2. Basic structure of pantograph [15]

The operation of pantograph and catenary system involves several physical fields such as mechanical, heat and electrical that require proper maintenance. A slight disturbance in these parameters will lead to significant changes in the performance of the system [4]. The operation of the pantograph centenary system can be analyzed using a damping model represented as Figure 3. Here, m_1, m_2 and m_3 refers to the mass of panhead, mass of inertial frames (lower arm and upper arm) respectively. On the other hand, parameters such as k_n(n=1,2), c_n(n=1,2), y_n and F refer to the stiffness between panhead and frames, the damping between frames and base or between pan-head and frames, vertical displacement of panhead and frames and uplift force respectively.

The damping model shown in Figure 3 can be expressed in terms of the following equation [3,17-18].

$$M\ddot{y} + C\dot{y} + Ky = F \tag{2.1}$$

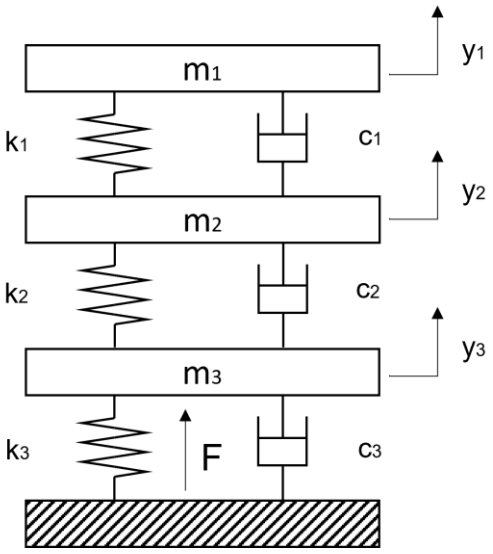

Figure 3. Pantograph Lumped Model [3]

where M, C and K correspond to mass, damping and stiffness matrices, respectively. The natural frequency (ω) of pantograph can be approximated by [3]

$$\omega^2 = \frac{K}{M} \tag{2.2}$$

Therefore, from equations (2.1) and (2.2), it can be seen that the mass of pantograph affects the uplift force and the nature frequency and thus, any change or modification in mass (for example adding a sensor) will change the original dynamic property of the pantograph.

The coupling mode of entire pantograph-catenary system can be represented in terms of Figure 4(a) while for easier analysis, the simplified model as shown Figure 4(b) can be considered. The equation (2.1) can now be rewritten as [19]

$$M\ddot{y} + C\dot{y} + K(t)y = F \tag{2.3}$$

where

$$K(t) = K_0\left(1 + \varepsilon\cos\left(\frac{2\pi v}{l}t\right)\right) \tag{2.4}$$

Here, K_0 , ε , l , v and t refer to the average stiffness of catenary, difference coefficient of elasticity in the catenary span, span length of catenary, train speed, and time. Therefore, the pantograph and catenary interaction gets affected by the speed of the train.

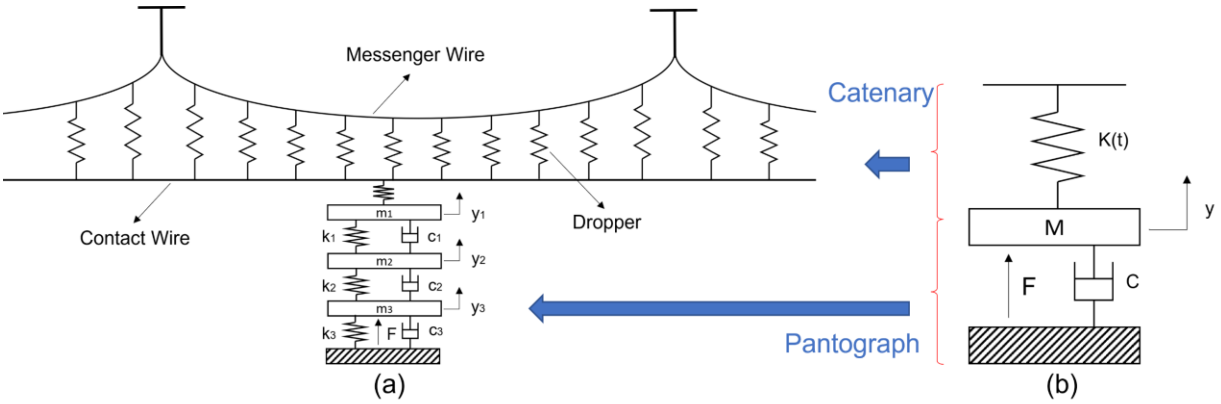

Figure 4. (a) Pantograph-catenary coupling model (b) Simplified model [19]

Apart from mass pantograph and speed of train, the pantograph catenary interaction also gets affected by several other factors such as aerodynamic force, geometry and the orientation of pantograph and direction motion of the pantograph. The major aerodynamic effect occurs due to the speed of train, orientation and working height of pantograph [2]. The drag and lift force of the pantograph gets affected by the profile of pan-head and the orientation of pantograph and this has been demonstrated by the wind tunnel experiment [20,21]. Furthermore, CFD model simulation shows that the collector uplift force also gets varied with the train speed [22]. Additionally, the zig zag motion of pantograph that arises due to the motion along lateral direction affects the stability of the pantograph. The convex nature of the surface of pantograph results in an air gap between the panhead and contact wire and the zig zag motion affect this air-gap thereby leading to the interruption in power supply [14].

In summary, the pantograph-catenary interaction gets affected by the motion along vertical and lateral direction.

2.2 Fabrication of Fiber Bragg Grating (FBG)

FBG consists of periodic modulation of refractive index in the optical fiber core and the modulated segment reflects a particular wavelength while transmitting other wavelengths [23]. The schematic of a typical fiber Bragg grating is shown in Figure 5.

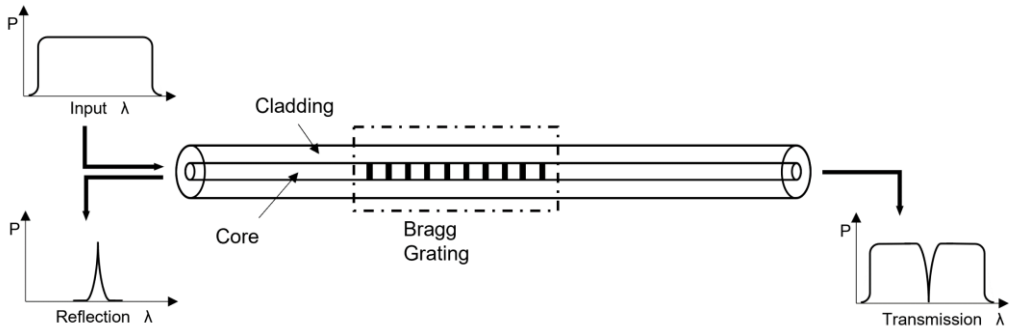

Figure 5. Reflection and transmission of light in fiber Bragg Grating [23].

The modulation in refractive index is accomplished using high intensity UV laser beam and photosensitive fiber where the change in index depends upon the doping concentration in fiber. The photosensitivity of the fibers is usually enhanced by low temperature hydrogen treatment prior to UV exposure [24,25]. Alternatively, periodic modulation can also be induced in non-photosensitive fiber by the use of femtosecond laser. Basically, the fabrication of FBG has been demonstrated using interferometry (holographic) and phase mask technique as well as point by point or line by line technique.

In interference technique, a beam splitter splits the incident laser beam into two and these two beams in turn are reflected by two mirrors and ultimately gets recombined on the fiber as shown in Figure 6(a). Recombination results in the formation of periodic fringes and this leads to the periodic change in the refractive index of the

fiber. The period of the grating is determined by the interference angle θ and wavelength of incident laser beam [26]. Therefore, the period can be tuned by rotating the mirrors thereby varying the angle θ. Several works have been reported on inscription FBGs using interferometry technique. FBG has been inscribed by in germanosilicate based optical fiber using UV laser-based interferometry technique at wavelength of 244nm [26]. Alternatively, the beam splitter in the conventional holographic set up has been replaced by a phase mask in a Talbot interferometric arrangement to inscribe grating in fiber as shown in Figure 6(b) [27]. A chirped phase mask that acts as a nonhomogeneous beam splitter generating nonhomogeneous periods on fiber has been used to inscribe chirped FBG [28]. A two-beam interferometer utilizing light from a deep ultraviolet femtosecond laser has been demonstrated to inscribe FBG in visible spectral range [29]. In order to reduce the alignment complexity, two electro-optical phase modulators (EOPMs) have been inserted between phase mask to get a fixed position of the recombined beams as shown in Figure 6(c) [30]. In this case the wavelength of grating can simply be tuned by controlling the EOPMs. All the works described above based on interferometry technique are vulnerable to mechanical vibration and require high spatial coherent beam as well as precise alignment of the optical system.

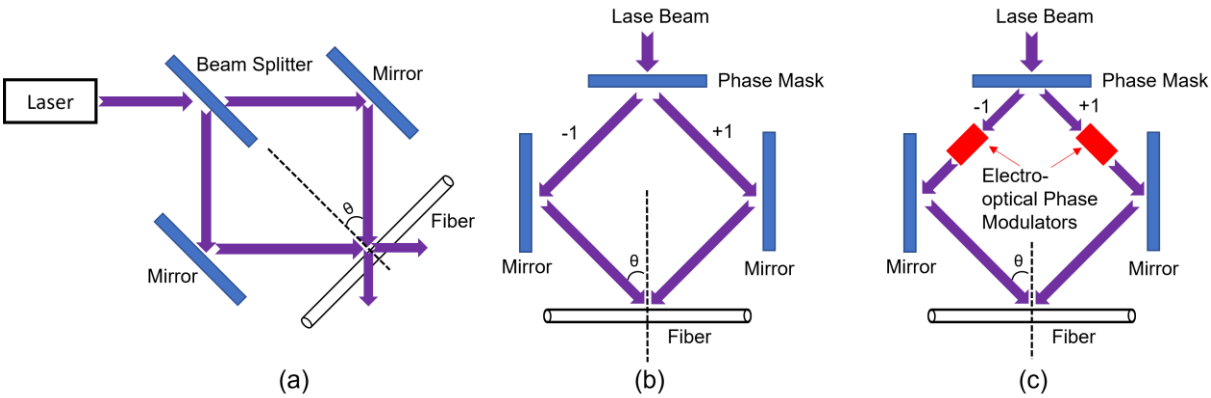

Figure 6. Fabrication of FBG using interference technique: (a) conventional [26] (b) with phase mask [28] and (c) with phase modulator [30].

Apart from interferometry, another inscription technique based on phase mask has been widely investigated. The schematic of the FBG inscription using phase mask is shown in Figure 7. The incident laser beam is transmitted through a phase mask and gets diffracted into beams of different orders. The ±1 order (that contain more than 35% of diffracted light) are made to interfere with each other on the fiber and this results in the periodic change in refractive index [31]. The diffracted beam is gradually scanned along the fiber to get FBG of desired length and peak intensity. This technique can be implemented with easier alignment of optical system and relaxes the stability as well as coherence requirement that are required in holographic technique. With this technique, the center wavelength of FBG can easily be tuned by changing the phase mask with different period. Because of the simple setup, phase mask technique has been widely used to inscribe different types of gratings in optical fiber. Several procedures have been developed to inscribe FBGs in fiber using the above technique. For example, the UV exposure time to inscribe FBG can be reduced by increasing the photosensitivity of doped fiber [32]. The long exposure time leads to the shift in center wavelength due to the DC index changes in the exposure region. Also, Kashyap et.al reported the apodising grating using phase mask technique by stretching the fiber during fabrication [33]. A technique to inscribe complex Bragg grating has been reported by Cole et.al where the velocity of the fiber has been tuned during beam scanning to tune the center wavelength of the grating [34]. Apart from these several other types of FBGs such as phase-shifted FBG [35], Tilted FBG [36] and Chirped FBG [37] have also been inscribed using phase mask technique. However, the use of UV laser with pulse duration of nanoseconds makes it mandatory to use photosensitive fiber for inscription of FBGs. Additionally, the polymer coating needs to be removed before inscription of FBG thereby reducing the mechanical strength of fiber. This issue can be addressed by using high power ultrafast laser with pulse width of few hundred femtoseconds. For example, chirped

FBG has been inscribed in non-photosensitive fiber using fs laser-based phase mask technique [38]. Inscription of tilted FBG has been carried out in fiber through the polyimide coating of the fiber using infrared femtosecond laser [39]. Furthermore, a highly birefringent phase-shifted FBG has also been inscribed using the above technique [40].

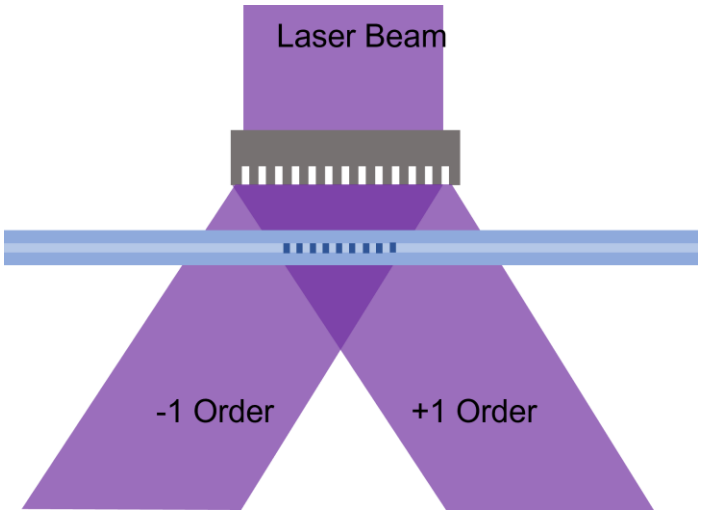

Figure 7. Schematic of phase mask technique.

However, inscription of FBGs involving either UV laser or femtosecond laser require phase mask of different periods to achieve peaks with desired wavelengths. This could be resolved using femtosecond laser-based point by point or line by line techniques. These techniques not only lead to inscribe FBGs of the desired wavelength but also do not require photosensitive fiber and removal of polymer coating. A detailed description of this technique is described in the following section.

2.3 Principle of Femtosecond Laser for FBG Fabrication

2.3.1 Femtosecond Laser-induced Breakdown and Damage Mechanisms

A femtosecond laser (fs laser) belongs to an ultrafast laser system that emits pulses with pulse duration ranging from few to hundred femtoseconds. A typical Gaussian pulse with duration $\Delta t < 500 fs$ is shown in Figure 8.

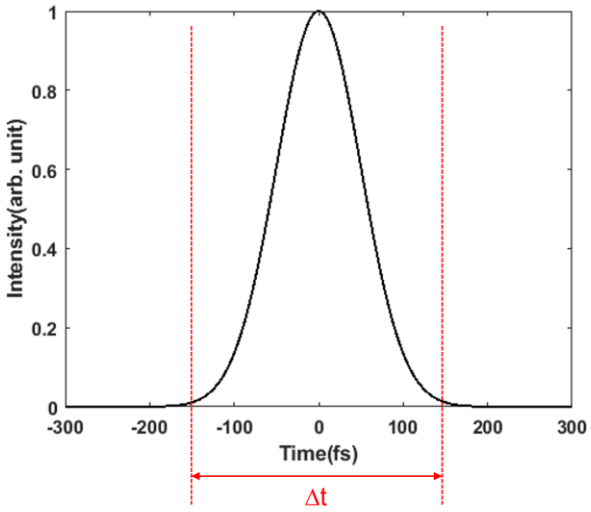

Figure 8. A typical femtosecond laser pulse with Gaussian shape.

The intense pulse from the fs laser can modify a dielectric structure permanently by means of nonlinear optical absorption mechanism [41]. Basically, the nonlinear absorption processes can be divided into three categories depending upon the energy of the incident laser. These are (a) Tunneling ionization, (b) Multiphoton ionization and (c) Avalanche ionization as illustrated in Figure 9.

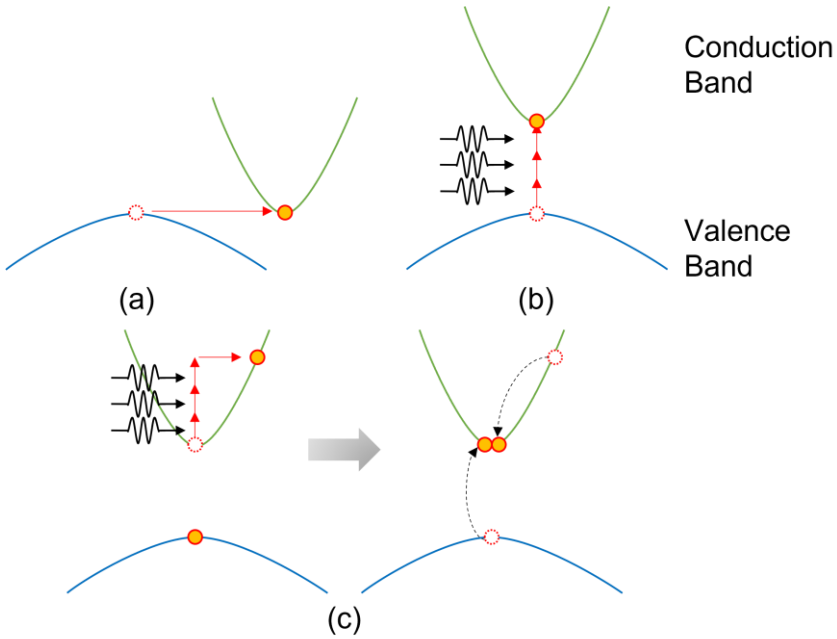

Figure 9. (a) Tunneling Ionization (b) Multiphoton ionization (c) Avalanche Ionization [42]

In tunneling ionization, the high electric field leads to the suppression of Coulomb well that in turn results in tunneling of the electrons from valence band (VB) to conduction band (CB). On the other hand, simultaneous absorption of m number of photons where $m\hbar\omega > E_g$ leads to multiphoton ionization process. Here, the number of m photons, where m is the integer that it should satisfy the minimum requirement, $\hbar$, ω , and E_g refer to the reduced Planck constant, laser frequency, band gap energy between valance and conduction band respectively [42]. The above two processes can compete with each other when the intensity of the laser pulse is high and this can be distinguished by Keldysh parameter [43]

$$\gamma = \frac{\omega}{e}\left[\frac{mcn\varepsilon_0 E_g}{I}\right]^{1/2} \tag{2.5}$$

where m and e refer to the reduced mass and charge of the electron while I , c , n, and ε_0 refer to laser intensity, velocity of light, refractive index of material and free space permittivity. For γ <1.5, the tunneling ionization is dominated while multiphoton ionization is dominated for γ >1.5. On the other hand, for $\gamma \approx 1$, both of these processes are dominated [44]. The process underlying the avalanche ionization is described as follows. A free electron in the CB accumulates energy by absorbing several laser photons. When this energy exceeds the minimum energy of CB by an amount more than the band gap, the electron can ionize another bound electron in VB thereby resulting in two electrons near the bottom of CB [42,44]. These two electrons undergo the same process leading to avalanche ionization. Therefore, seed electrons are required for avalanche ionization and these can be provided either by thermally excited carriers, tunneling ionization or multiphoton ionization.

The interaction of the femtosecond pulse with the material basically leads to three types of modification in the material namely (I) smooth index change, (II) formation

of nanograting, and (III) formation of nanovoid [44]. The rapid cooling of melted glass from high temperature leads to the smooth change in refractive index for low pulse energy above threshold. However, for intermediate laser energy (i.e., pulse energy of ~150nJ-500nJ) there is formation of nanograting in the irradiated volume region [45]. The mechanism behind this phenomenon can be attributed to the interference between the incident light field and bulk electron plasma wave induced by the incident laser field. On the other hand, for high pulse energy (>500 nJ), the incident laser field generates shockwave that exceeds the internal pressure within the focal volume. This leads to micro-explosion in the focal volume thereby producing a void surrounded by high index region [46]. The phenomenon of smooth refractive index change can be utilized to write waveguide or inscribe grating in fiber by point by point or line by line technique [47] while the phenomenon of nanovoid formation can be used for structure modification of material for sensing applications or microfluidic channels fabrication.

2.3.2 Femtosecond Laser Inscribed Fiber Bragg Gratings (FBGs)

The smooth modification of refractive index at the focus spot of the fs laser can be employed to inscribe waveguides and gratings in fiber. The inscription of grating in fiber could be achieved either by point by point (PbP) or line by line (LbL) technique. A typical set up to inscribe FBG using fs laser based PbP technique is shown in Figure 10. Light from femtosecond laser is passed through a halfwave plate, polarizer and quarter wave plate before being reflected from a dichroic mirror and focused onto the fiber using a microscope objective (MO). The fiber is kept on a high precision translational stage and it is illuminated with an LED. The reflected light from the fiber is transmitted through the MO and dichroic mirror and gets reflected by another mirror onto the CCD thereby enabling to monitor the inscription in real time. The fiber is kept on a glass slide with its two-end fixed. A drop of index

matching oil is placed on the fiber to remove the curvature error of the fiber due to its cylindrical geometry. The velocity of the translation is precisely controlled in all three directions. The grating period is governed by adjusting the velocity of the translational stage and the repetition rate of the pulse.

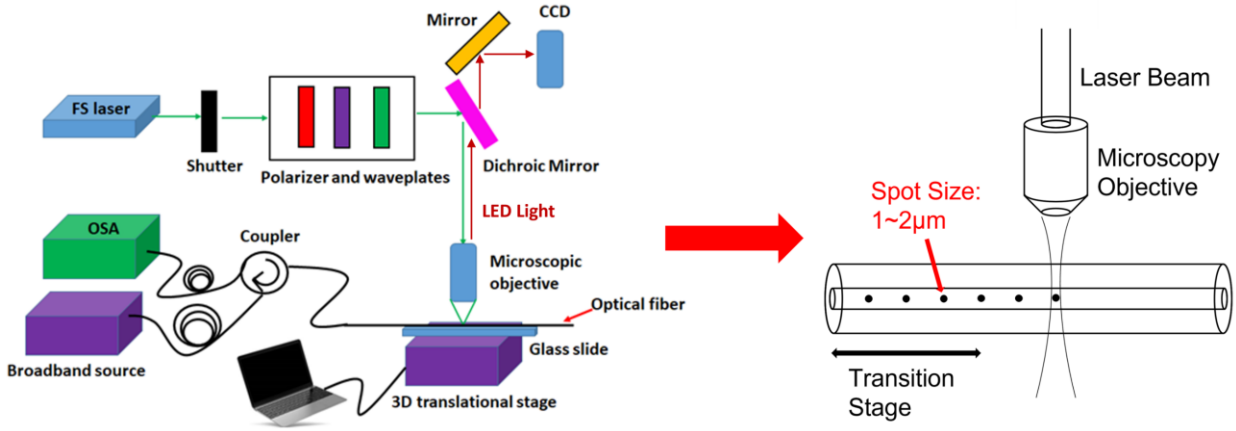

Figure 10. Basic set up for the inscription of point-by-point grating using femtosecond laser.

Several types of FBGs have been inscribed using PbP technique for different applications. Martinez et al. have reported direct writing of FBG by fs laser based PbP technique and the reflectivity of different orders of gratings have been analyzed in his work [48]. Here, the second order grating has been found to have higher reflectivity compared to that of first order grating owing to the overlapping between the spots at the focused region of the laser. With higher laser pulse energy, it has been possible to inscribe PbP grating through the coating thereby enhancing the robustness of the fiber for sensing applications. For example, FBG inscribed through the coating using infrared fs laser has been found to withstand larger strain compared to the bare fiber [49]. A variety of complex gratings such as amplitude- and phase-modulated sampled gratings and gratings with controlled bandwidth have also been inscribed using PbP technique [50]. Williams et al. have reported the inscription of eighth-order grating with bandwidth of 30 pm for application in Q-switched fiber laser-based system [51]. A DFB fiber laser based on FBGs inscribed by fs laser has

been found to have a spectral line width around 17kHz [52]. Furthermore, inscription of five parallel FBGs in the fiber core with each having different peak wavelengths has been demonstrated where there has been increase in reflectivity and FWHM for parallel gratings with same peak wavelengths [53]. Moreover, FBG has been inscribed in the cladding close to the core-cladding interface and resulting offset FBG based system has been demonstrated for bending and shape sensing [54]. Besides these, fs laser has also been used to inscribe two FBGs in a tapered fiber for the demonstration of a tunable fiber notch filter based tension and temperature sensor [55]. The aforementioned gratings based on smooth modification in refractive index cannot be used for high temperature applications. However, fibers inscribed with fs laser based nanograting has been found to have long-term stability for extreme high temperature environment (>1000ºC) applications [56].

The size and morphology of the laser induced spots determine the scattering loss and reflectivity of the gratings inscribed by PbP technique [57,58]. Stronger transmission losses at wavelengths smaller than 400 nm due to Mie scattering effect have been reported [57]. In one of the studies, the scattering loss in gratings written with PbP technique have been found to be 19% which is higher than traditional gratings written using UV laser [58].

The PbP based inscription technique offers fast fabrication but requires precise alignment of optical fiber. On the other hand, inscription of gratings using LbL technique does not get affected by the misalignment of fiber although the inscription duration is much longer (e.g. 3mm grating spends < 10 seconds with PbP while > 30 minutes with LbL). In this technique, the inscription of each line is carried out by moving the fiber in transverse direction with respect to the incident laser beam for each line and this process is repeated several times along the longitudinal direction. The schematic of the LbL based inscription is shown in Figure 11.

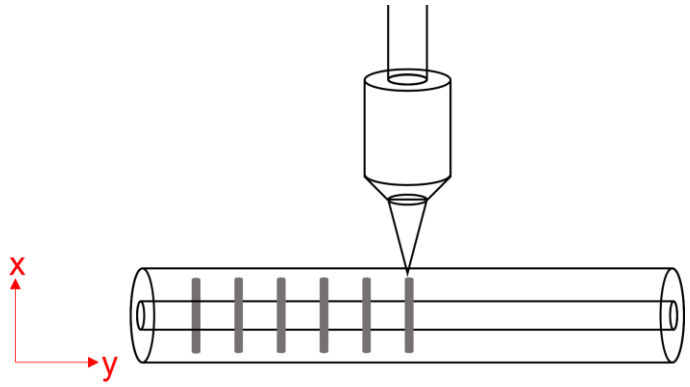

Figure 11. Femtosecond laser-based inscription of FBG by line-by-line technique.

Several types of FBGs have been inscribed using LbL technique for different applications. A significant lower polarization dependent loss compared to PbP technique has been demonstrated in gratings written using fs laser based LbL technique [59]. LbL based fiber Bragg grating with phase shift of $\pi/2$, π and $3\pi/2$ have been fabricated by controlling the pitch of the lines [60]. Xizhen et al. (2018) have demonstrated the inscription LbL gratings in single-crystal sapphire fibers using femtosecond laser [61]. These gratings have been found to have reflectivity of 6.3% and could withstand a high temperature ~1600ºC. Furthermore, LbL technique has also been utilized to inscribe aperiodic FBGs that could be used as filter elements [62]. Chernikov et al. have demonstrated inscription of LbL gratings through the polymer coating and resulted reflection spectra have been found to have a set of pronounced peaks around the center wavelength that can be attributed to several factors such as non-uniform laser pulse energy, non-uniform displacement of optical fiber, non-uniform modification of medium [63].

2.4 Theory of Fiber Bragg Grating (FBG)

The refractive index change induced in optical fiber by the incident laser beam can be expressed as [64]

$$\Delta n(z) = \Delta n_{DC}(z)\left[1 + v\cos\left(\frac{2\pi}{\Lambda}z + \phi(z)\right)\right] \tag{2.6}$$

where $\Delta n(z)\ and\ \Delta n_{DC}(z)$ refer to the refractive index change along the length of the fiber and "dc" index change spatially averaged over a grating period. The parameters Λ, v and $\phi(z)$ refer to the period of grating, fringe visibility and grating chirp respectively. The schematic of index modulation and interaction of light with the grating are illustrated as Figure 12 and Figure 13 respectively. In Figure 13, a transverse mode gets reflected by Bragg grating with angle θ_1 into the mode traveling in the opposite direction with angle θ_2 .Here m and n_{co} refer to the diffraction order and refractive index of fiber core respectively.

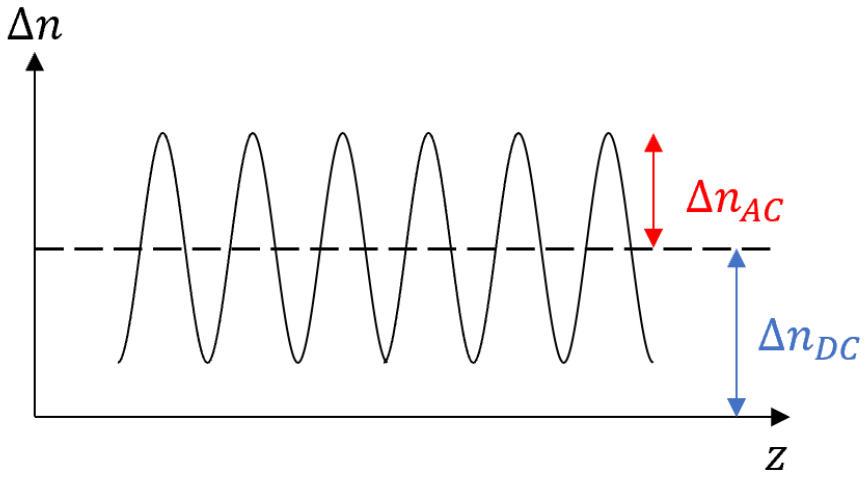

Figure 12. Refractive index modulation

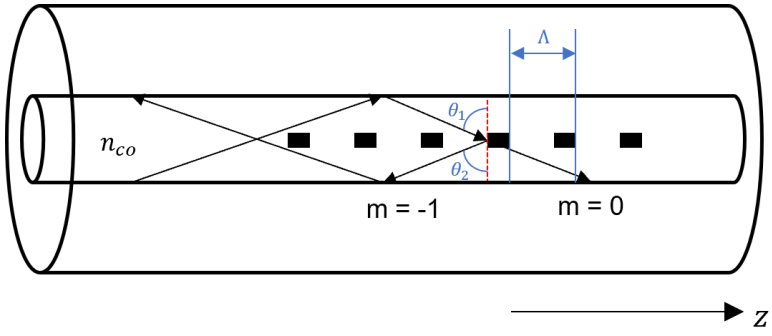

Figure 13. Diffraction of light from the refractive index modulated region.

The propagation constant of the mode guided through the core of the fiber can be expressed as [64]

$$\beta = \left(\frac{2\pi}{\lambda}\right) n_{eff} \tag{2.7}$$

where n_{eff} refers to the effective refractive index and $n_{eff} = n_{co}\sin(\theta)$ and θ can be θ_1 or θ_2.

Thus, the grating equation for guided modes is expressed as

$$\beta_2 = \beta_1 + m\left(\frac{2\pi}{\Lambda}\right) \tag{2.8}$$

where β_1 and β_2 are propagation constants of forward and backward propagating light respectively. Then, the resonant wavelength can be obtained by substituting equation (2.8) into (2.7)

$$m\lambda = \left(n_{eff,1} + n_{eff,2}\right)\Lambda \tag{2.9}$$

If both modes have same effective indices, then $n_{eff,1} = n_{eff,2}$. Then equation (2.9) will be expressed as

$$m\lambda = 2n_{eff}\Lambda \tag{2.10}$$

For PbP or LbL inscribed grating, the pitch of grating (Λ) can be expressed as

$$\Lambda = \frac{v}{f} \tag{2.11}$$

where v is stage velocity and f is the pulse repetition rate. Therefore, Equation (2.10) can be modified as [65]

$$\lambda = \frac{2n_{eff}v}{mf} \tag{2.12}$$

where m is the order of grating.

The above equations (2.7)-(2.10) are used to determine the resonant wavelength of Bragg grating. To obtain quantitative information about the diffraction efficiency (e.g. reflectivity) and spectral (e.g. bandwidth) dependence of fiber grating, coupled-mode theory is an excellent mathematical tool to analyze it.

Coupled mode theory is a mathematical tool that is being used for the analysis of electromagnetic wave propagation and its interaction with media. The operation of existing devices and systems as well as some new concepts and designs can be explained by this mathematical approach [66]. Coupled mode theory was utilized to analyze microwave traveling-wave tube by Pierce [67]. The coupled mode theory was further developed to describe the mode conversion in microwave waveguide and the periodic waveguide structure in the 1960's [68-71]. Marcuse (1971) developed the coupled mode theory for two parallel dielectric waveguides and this can also be applied to dielectric waveguides of arbitrary shape and arbitrary distribution of refractive index [72]. The coupled mode theory was also applied for modeling and analysis of periodic dielectric waveguide by Stoll et al. (1973) [73]. The coupled-mode equations for Bragg grating are expressed as [64,74]

$$\frac{dR}{dz} = i\hat{\sigma}R(z) + i\kappa S(z) \tag{2.13}$$

$$\frac{dS}{dz} = -i\hat{\sigma}S(z) - i\kappa^{*}R(z) \tag{2.14}$$

where

$$R(z) = A(z)e^{i\delta z - \phi/2} \tag{2.15}$$

$$S(z) = B(z)e^{-i\delta z + \phi/2} \tag{2.16}$$

In these equations, $A(z)$ and $B(z)$ are the amplitudes of the modes traveling in $+z$ and $-z$ direction, κ is the "ac" coupling coefficient, $\hat{\sigma}$ is a general "dc" self-coupling coefficient, and the detuning δ is independent of z for all grating. These parameters are defined as

$$\hat{\sigma} \equiv \delta + \sigma - \frac{1}{2}\left(\frac{d\phi}{dz}\right) \tag{2.17}$$

$$\delta \equiv \beta - \frac{\pi}{\Lambda} \tag{2.18}$$

For single-mode Bragg grating, the "dc" coupling coefficient σ and "ac" coupling coefficient κ can be expressed as

$$\sigma = \frac{2\pi}{\lambda}\Delta n_{DC} \tag{2.19}$$

$$\kappa = \kappa^* = \frac{\pi}{\lambda}\Delta n_{AC} \tag{2.20}$$

where Δn_{DC} refer to the "dc" index change spatially averaged over a grating period, Δn_{AC} refer to the "ac" induced index change. For a uniform grating, the factors κ, σ and $\hat{\sigma}$ are constant since Δn_{DC} is constant and $d\phi/dz = 0$.

The reflectivity of the uniform Bragg grating can be expressed as [75,76]

$$r = \frac{\sinh^2\left(\sqrt{\kappa^2 - \hat{\sigma}^2}L\right)}{\cosh^2\left(\sqrt{\kappa^2 - \hat{\sigma}^2}L\right) - \frac{\hat{\sigma}^2}{\kappa^2}} \tag{2.21}$$

where L refers to the length of grating. When $\hat{\sigma} = 0$, the maximum reflectivity for a given wavelength can be obtained from equation (2.17) -(2.20)

$$\lambda_{max} = \left(1 + \frac{\Delta n_{DC}}{n_{eff}}\right)\lambda_D \tag{2.22}$$

where $\lambda_D = 2n_{eff}\Lambda$ (first order grating).

Therefore, the maximum reflectivity will be [64]

$$r_{max} = \tanh^2(\kappa L) \tag{2.23}$$

The bandwidth of uniform Bragg grating that between first zeros on either side of center Bragg wavelength is [64,77]

$$\Delta\lambda = \frac{\lambda^2}{n_{eff}}\sqrt{\frac{\kappa^2}{\pi^2} + \frac{1}{L^2}} \tag{2.24}$$

According to equation (2.20), the reflectivity of center wavelength depends on the length of grating and the "ac" coupling coefficient that that in turn depends upon the index changes in fiber core. Thus, for a strong grating where $\kappa^2 \gg 1 \,/\, L^2$, the equation (2.24) can be simplified to

$$\frac{\Delta\lambda}{\lambda} \rightarrow \frac{\Delta n_{AC}}{n_{eff}} \tag{2.25}$$

For week grating where $\kappa^2 \ll 1 \,/\, L^2$, equation (2.24) can be

$$\frac{\Delta\lambda}{\lambda} \rightarrow \frac{2}{n_{eff}L} \tag{2.26}$$

Equation (2.22) and (2.23) show the bandwidth of Bragg grating can be controlled by adjusting the index change of strong grating or the length of weak grating.

2.4.1 FBG Applications

FBG can be used to monitor several important parameters such as strain, curvature, and temperature. The applied strain induces physical elongation (changing the grating pitch/period) and change in index due to the photoelastic effect. On the other hand, the change in temperature induces inherent thermal expansion as well as

change in refractive index. The shift in wavelength of Bragg grating can be expressed as [78]

$$\Delta\lambda_B = \lambda_B\left(\left\{1 - (\frac{n^2}{2}[P_{12} - \vartheta(P_{11} + P_{12})]\right\}\varepsilon + \left[\alpha + \frac{1}{n}\left(\frac{dn}{dT}\right)\right]\Delta\mathrm{T}\right) \quad (2.27)$$

where $\lambda_B = 2n_{eff}\Lambda$. The parameters ε, P_{ij} ϑ, α and ΔT refer to the applied strain, Pockel's coefficients of stress-optic tensor, Poisson's ratio, thermal expansion coefficient of fiber material and change in temperature. The strain and temperature induced shift in Bragg wavelength can be expressed as [79]

$$Temperature: \Delta\lambda_B = \lambda_B(\alpha + \xi)\Delta T \quad (2.28)$$

$$Strain: \Delta\lambda_B = \lambda_B(1 - p_E)\varepsilon \quad (2.29)$$

where $\xi = (1/n)(dn/dT)$ is the thermal-optic coefficient and $p_E(= (n^2/2)[P_{12} - \vartheta(P_{11} + P_{12})])$ is the photoelastic coefficient. For silica fiber, the typical value of p_E is approximated to 0.22. The measured strain response at constant temperature and thermal response at constant strain for conventional single-mode fiber (SMF) can be expressed as [78]

$$\frac{1}{\lambda_B}\left(\frac{\delta\lambda_B}{\delta\varepsilon}\right) = 0.78 \times 10^{-6}\mu\varepsilon^{-1} \quad (2.30)$$

$$\frac{1}{\lambda_B}\left(\frac{\delta\lambda_B}{\delta T}\right) = 6.67 \times 10^{-6}{}^{\circ}\mathrm{C}^{-1} \quad (2.31)$$

2.5 Fiber Bragg Grating (FBG) Accelerometer

Modern engineering systems such as railway and aircraft require on-time health monitoring and maintenance to ensure security and stability [80]. Most of the faults in these systems lead to abnormal vibration and therefore the analysis of the vibration/acceleration signal plays an important role in reducing economic loss and

maintaining the health of the system by avoiding accidents [81]. The conventional accelerometer based on capacitive or piezoelectric principles faces many challenges in harsh conditions involving strong electromagnetic field [82]. These issues can be addressed by usage of FBG based sensors due to its compactness and immunity to electromagnetic interference [83]. Usually, the vibration signal has been measured in terms of acceleration by fixing the FBG sensor on the surface of a cantilever beam as shown in the schematic in Figure 14. The deformation of the beam due to the vibration induces strain on the FBG fixed on its surface and the vibration signals from the system can be analyzed by monitoring the shift in center wavelength of

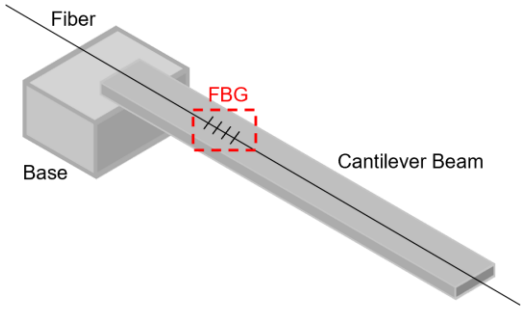

Figure 14. Schematic of cantilever beam-based accelerometer.

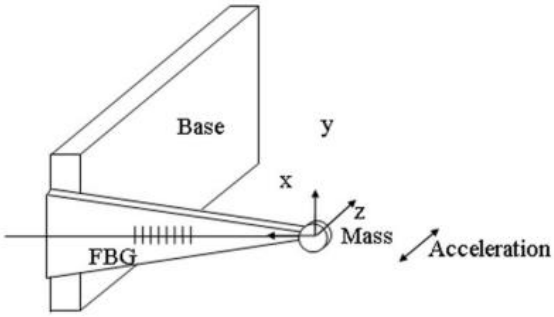

Figure 15. Triangular cantilever beam [85]

FBG [82,84]. In the cantilever beam system shown in Figure 14, the strain induced along the beam due to bending is non-uniform thereby inducing nonuniform strain on the FBG. This results in chirping of the FBG spectrum which in turn broadens

the spectrum making it difficult to monitor. Chunzheng Shi et.al have proposed a triangular shape cantilever beam to improve the strain distribution on the FBG thereby reducing the chirp effect as shown in Figure 15 [85]. A short FBG based accelerometer has also been proposed to reduce the chirping effect [86]. Apart from this, FBG has also been embedded inside a 3D printed cantilever beam [87] for vibration measurement. In the above-mentioned sensors, the FBG peak also gets affected by the change in surrounding environmental temperature. This has been addressed by installing two FBGs in opposite directions as shown in Figure 16 [88] Here, the shift in peak wavelength of FBGs due to change in temperature are same while the strain induced wavelength shifts are different. The sensitivity of the two-FBG based accelerometer have been reported to be 106.5pm/g and 109pm/g at 80Hz.

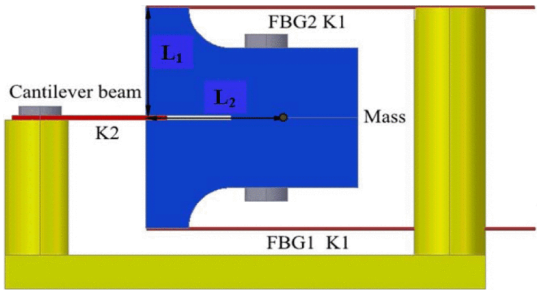

Figure 16. Cantilever beam-based accelerometer using two FBGs [88]

The aforementioned structures can only be used for one dimensional acceleration measurement. In order to measure acceleration in 2 axes, an FBG-inscribed multicore fiber has been reported for two-dimensional acceleration monitoring which has exhibited a high sensitivity [89]. However, the FBGs were inscribed by UV illumination, where the stripped coating weakens the mechanical strength of the accelerometer. On the contrary, inscription of FBGs through the acrylate coating can be achieved using a femtosecond laser thereby keeping the mechanical strength intact. FBGs have been inscribed in the claddings of various fibers using femtosecond lasers for two-axis accelerometer designs [90-92]. For example, an

FBG inscribed in the cladding near the core of a single-mode fiber (SMF) has been introduced for intensity-based two-dimensional acceleration detection [90]. Moreover, a cladding-FBG in a thin core fiber and an eccentric FBG inscribed close to the core/cladding interface have been reported for orientation-dependent acceleration measurements [91,92]. However, the presence of a tapered region for coupling between the core and cladding leads to a high reflection loss as well as poor mechanical stability [92]. In order to address these issues, FBGs have also been inscribed in a multiple-cladding fiber using a femtosecond laser and a phase mask [93,94]. But the drawbacks such as increased fabrication complexity and long fiber length limit its practicality. Many other mechanical designs have also been proposed for two axis acceleration measurement. For example, two FBGs have been installed along two orthogonal directions in a cylindrical block that provides symmetrical mechanical properties in all directions (Figure 17). The direction of vibration has been analyzed by simple algebra based calculations with sensitivity being 13.1pm/g and 12pm/g at 300Hz along X- and Y-axes respectively [95]. Furthermore, Li Wei et.al have demonstrated a temperature insensitive accelerometer for two-dimensional acceleration measurement using 4 FBGs as shown as Figure 18 [96]. The 4 FBGs have been installed along ±X- and ±Y-axes and each of ±X/Y pair have been used to cancel the wavelength shift induced by temperature. The response of the sensor has been analyzed for frequencies ranging from 20Hz to 600Hz with sensitivity being 40pm/g for both axes.

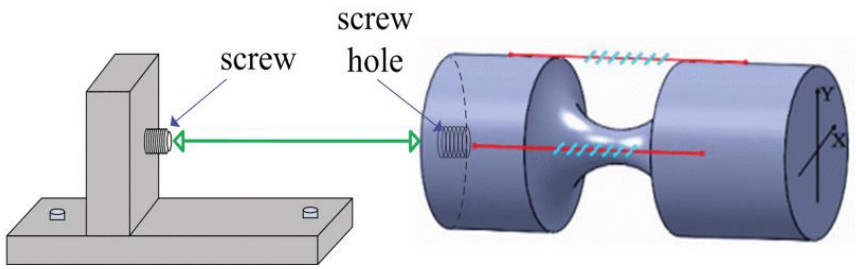

Figure 17. FBG based 2D accelerometer [95]

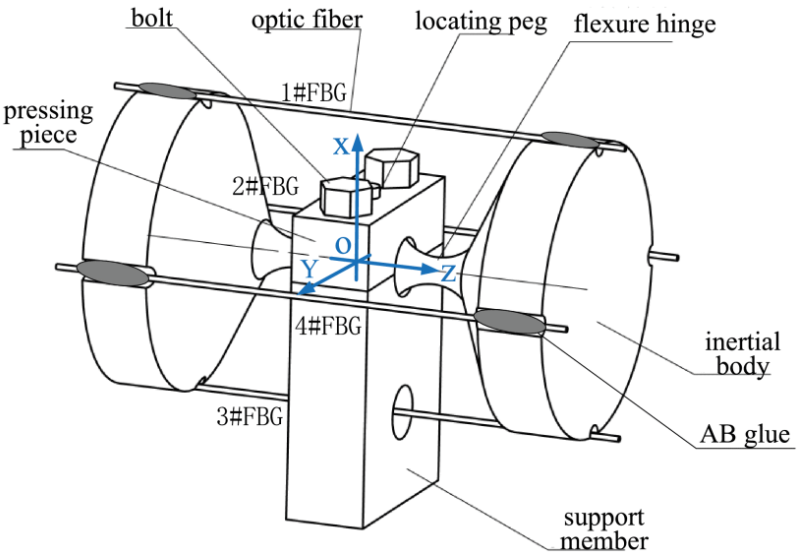

Figure 18. Temperature insensitive 2D FBG accelerometer [96]

Apart from one and two dimensional, investigations have also been carried out for three-dimensional acceleration measurement. Hui Wang et.al have proposed a 3D FBG accelerometer based on two pair of hinges as shown as Figure 19 [97]. The two side hinges were used for the X- and Y-axis vibration (sensitivity of 107.2pm/g and 145.9pm/g at 100Hz along X- and Y-axes) while the upper and lower hinges form a spring-like structure that were used to compress and relax along Z-axis (sensitivity of 27.7pm/g at 100Hz).

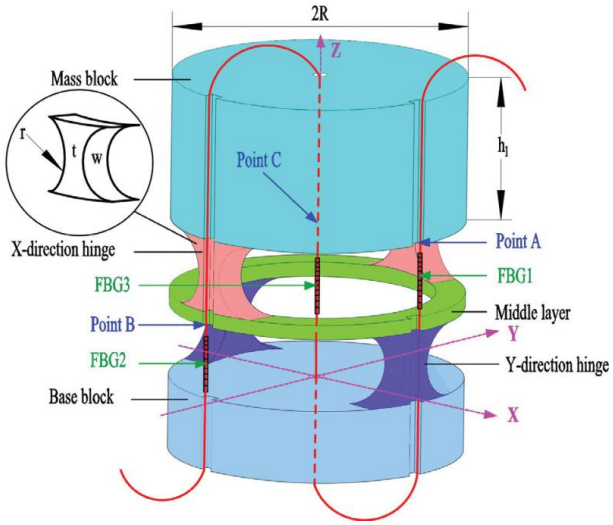

Figure 19. Schematic of multi-axis based FBG accelerometer using two hinges [97]

Although FBG based sensors are compact and lightweight, the use of transducers makes the entire system bulky. Fender et.al have reported a 2-axis FBG accelerometer based on four core multicore fiber without the need of additional transducer as shown in Figure 20 [98]. Here, each of the two diagonal cores form a differential pair and the operational principle is same as that described in [96].

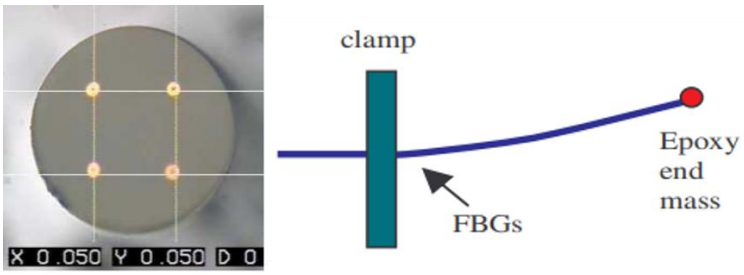

Figure 20. Multicore fiber based FBG accelerometer [98]

Furthermore, an FBG fixed on an isosceles triangular cantilever with high natural frequency has been demonstrated for acceleration measurement as shown in Figure 21 [99]. The proposed accelerometer has a small size of 7mm x 6mm x 2mm and weight of 0.82g with sensitivity of 0.48pm/g at 1000Hz while the resonant frequency has been around 8193Hz.

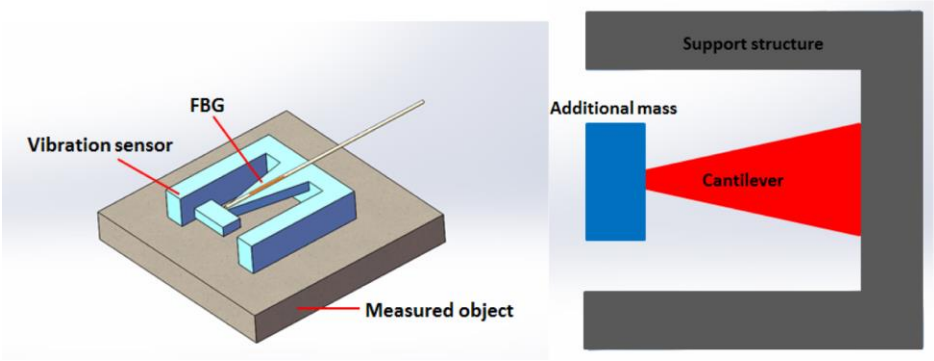

Figure 21. Triangular cantilever structure for acceleration measurement [99]

The use of FBG in place of traditional electrical sensors in some practical applications has also been investigated. For example, FBG based sensor has been utilized to monitor the pantograph–overhead line interaction in railway system and

the results indicated a good agreement between optical and electric signals [13]. In this case, the electric sensor could only be used with particular precautions due to the high electromagnetic disturbances of pantograph system. Kerstin et.al. have developed a compact (Weight about 50 grams) FBG based sensor for pantograph-catenary system monitoring where the FBG could detect the fast change in contact force [12]. An FBG based S-shaped load cell has also been demonstrated for contact force measurement in pantograph-catenary system [11]. Furthermore, a load cell with FBG sensor has been designed for active pantograph contact force measurement with the operational frequency range being 0-10Hz [100].

The above discussions demonstrated the potential of FBG based sensor for acceleration measurement in pantograph-catenary system with excellent performance in various operational frequency ranges. However, the bulky designs affect the dynamic property of pantograph while the removal of protective coating makes the FBG based sensor fragile. Therefore, a compact, robust, and mechanically stable FBG based accelerometer would be a better choice for pantograph-catenary system.

2.6 Summary

In this chapter, a review of the pantograph-catenary system interaction, principle of femtosecond laser for FBG fabrication and the theory of FBGs are presented. A thorough study of various fabrication techniques that have been followed for FBGs has been carried out. Among these, femtosecond laser-based technique offers the flexibility to inscribe the FBG of any order by controlling the speed and laser power without the requirement of photosensitivity fiber and phase mask as well as removal of polymer coating of the fiber. These features improve the robustness of FBG-based sensor that it can withstand the higher stress compared to the bare fiber. Finally, a detailed review based on the utilization of FBGs for various types of accelerometers

followed by their application for pantograph-catenary system have been carried out. The review indicates that accelerometers based on FBGs have many specific advantages such as compact size, utility in harsh environmental conditions along with multi-dimensional sensing capability. The reported sensors for pantograph-catenary system are either bulky or fragile. Therefore, a compact and robust accelerometer based on FBG is required to be developed for pantograph-catenary system.

Chapter 3. Stress Analysis for Cantilever based Accelerometer

In this chapter, the distribution of stress along the cantilever beam structure is analyzed using FEM based simulation technique (COMSOL). The analysis helps in finding a suitable position of the FBG along the optical fiber to ensure optimum performance for vibration sensing. The simulation results will be utilized to design and fabricate a vibration sensor based on multicore fiber as well as validate the experimental results. The geometry model of the optical fiber-based cantilever structure used for simulation is shown in Figure 22.

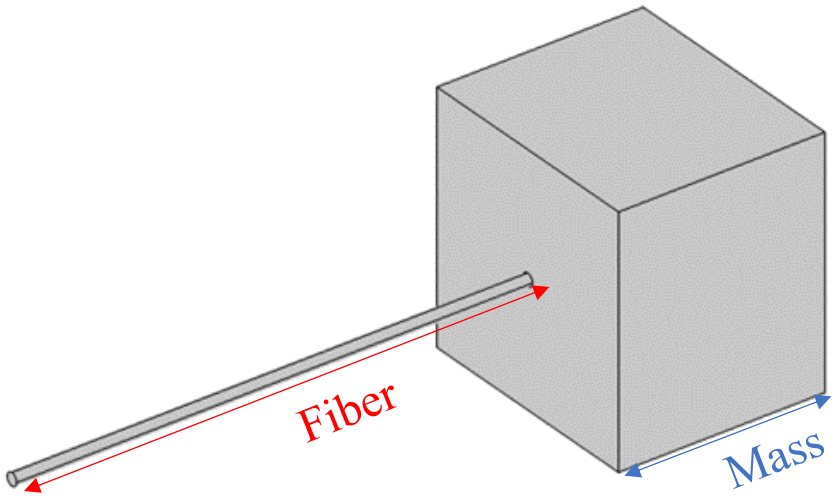

Figure 22. Schematic of the geometry of cantilever structure.

The stress analysis is carried out in static as well as dynamic mode. In static mode, the applied force on the cantilever structure is kept constant and stress distribution along the cross section as well as length of optical fiber is analyzed. On the other hand, in dynamic mode, the applied force changes with time thereby leading to the variation in displacement as well as stress with time. In this case, the stress distribution along the cross section of optical fiber at a specific position is analyzed.

3.1 Static Analysis

Table 1. Dimensions of Model and Material Parameters

	Length	Diameter /Height	Density	Young's modulus	Poisson's ratio
Fiber (SiO_2)	2mm-10mm	125um	2200kg/m^3	70 GPa	0.17
Mass (Plastic-PBT)	2.35mm	2mm	1380kg/m^3	3 GPa	0.406

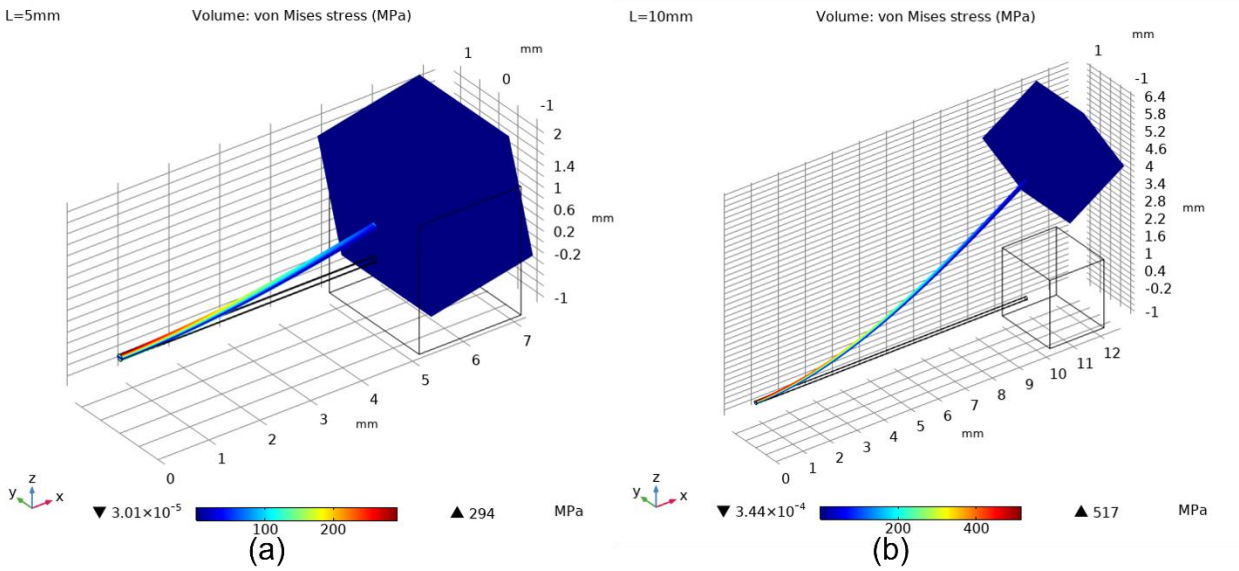

Figure 23. Bending of cantilever with beam length of (a) 5mm. (b) 10mm

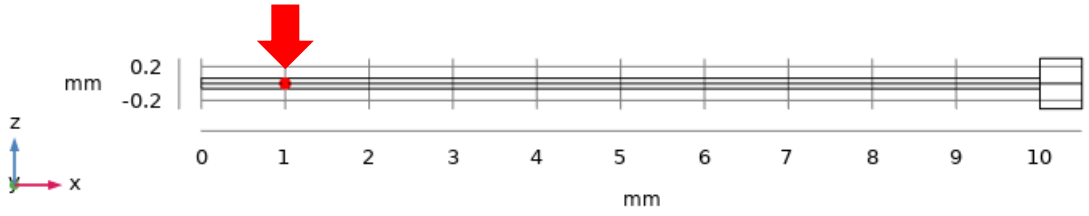

Figure 24. Position of point(x=1mm) for evaluation of stress.

The parameters of the optical fiber-based cantilever structure used in this model are listed in Table 1. The mass at the tip of cantilever and the force applied to bend the fiber were fixed at 15mg $((2.35mm)^2 \times 2mm \times 1380kg/m^3)$ and 0.01N respectively while the length of fiber was varied from 2mm to 10 mm. In order to

ensure accuracy, the mesh element size was set to “Extra fine”. The resulting bending and stress distribution along the fiber with length of 5 mm and 10 mm for a given applied force are shown in Figure 23. As can be seen from the figure, the longer beam has larger displacement at the tip. Thereafter, the displacement at a specified position (x=1mm, see Figure 24) for variation in length of optical fiber is evaluated. As can be seen from Figure 25, the displacement increases linearly with length of fiber. Furthermore, the stress at the specified positions such as x=200µm, 600µm and 1000µm for different beam length are also plotted in Figure 26. As can be seen from the figure, the stress is higher at x=200 µm and it increases linearly with beam length at a given position of analysis.

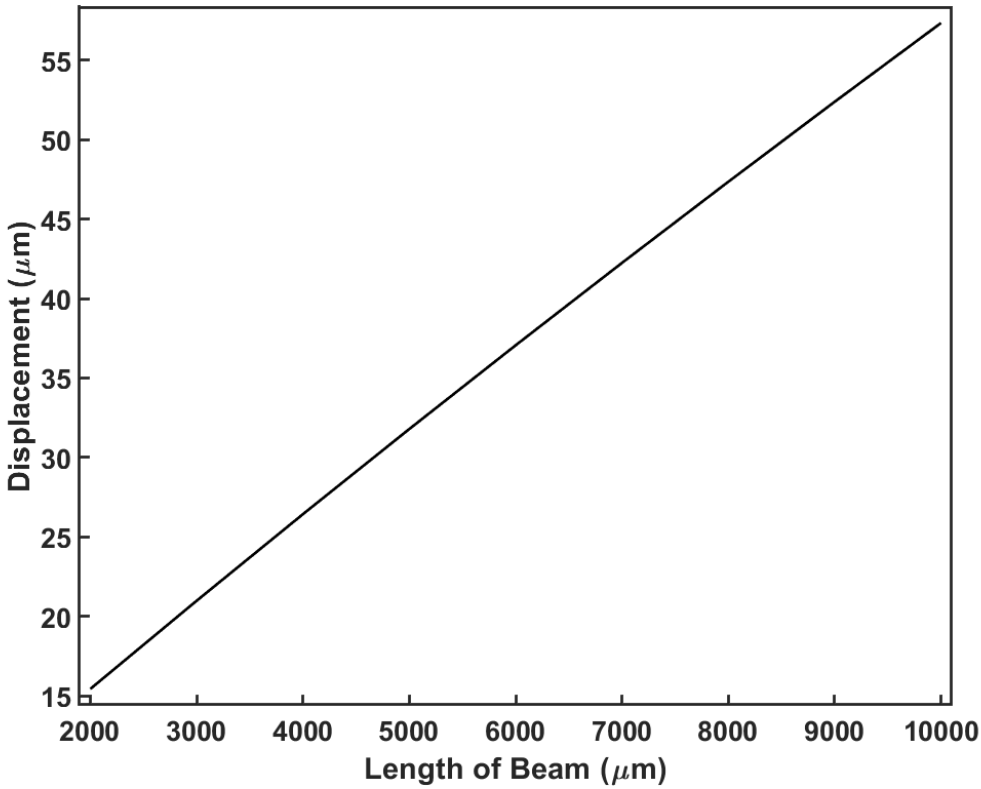

Figure 25. Displacement of the point(x=1mm) with beam length for a given applied force.

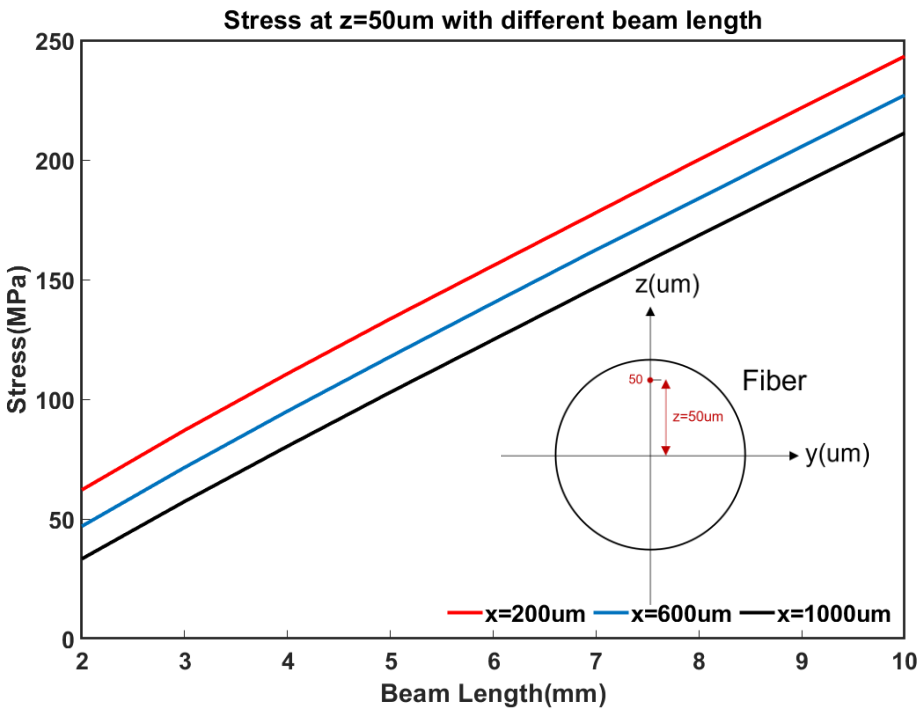

Figure 26. Variation of stress varied with length of beam at position x=200μm(red), 600μm(blue), x=1000μm(black).

The above response of the cantilever beam can be explained using equation (3.1) [101]

$$w(x) = \frac{Px^2(3L - x)}{6EI} \tag{3.1}$$

where *w*, *P*, *L*, *E*, and *x* refer to displacement, applied pressure at the tip, beam length, Young's modulus and beam position respectively. *I* refers to moment of inertia that can be defined by

$$I_y = \int x^2 dA \tag{3.2}$$

where x is the perpendicular distance from y-axis to the element dA (Figure 27 (a)).

For solid circular cross section (Figure 27 (b)), equation (3.2) can be written as

$$I_y = \int_0^{2\pi} \int_0^r \big(rcos(\theta)\big)^2 r dr d\theta \tag{3.3}$$

$$= \frac{\pi r^4}{4}$$

where r is the radius of the circle.

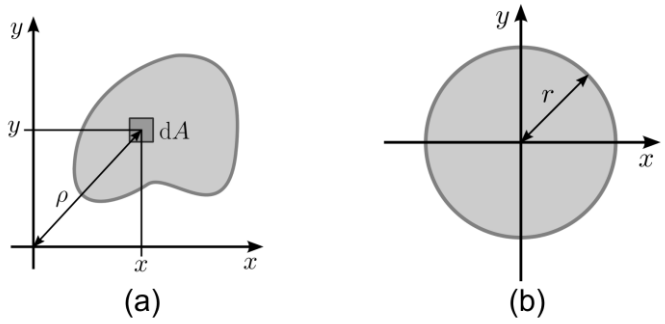

Figure 27. (a) A small element *dA* on cantilever (b) solid circular cross section.

Furthermore, the stress at any position of the beam with symmetrical cross-section can be expressed by [101]

$$\sigma = \frac{Mz}{I} \tag{3.4}$$

where σ, z, and M refer to stress, offset from the neutral axis to a point of interest, and bending moment respectively. *M* can be expressed as

$$M = EI\left(\frac{d^2w}{dx^2}\right) \tag{3.5}$$
$$= P(L - x)$$

Therefore, from the above equation, it can be concluded that the stress at any position along the fiber increases with an increase in length of the fiber. Also, the stress is higher at positions closer to the fixed point or farther away from tip of cantilever.

The analysis of stress distribution along the fiber length is followed by the evaluation of stress along the fiber cross section. The positions z=32.5µm, 40µm and 50µm along the cross sections are considered for analysis. The reason for considering

z=32.5 µm is the exact matching of this pitch with the available 3-core fiber. Furthermore, considering the symmetry of the fiber, the analysis has been confined to half of the total fiber area. Figure 28 (a)-(d) show the stress distribution along the fiber cross section for different beam lengths. As can be seen from these figures, the stress is lower at positions closer to the center of the fiber (z=0) and increases gradually towards the circumference of the fiber. Furthermore, for a given position along the cross section, the stress increases with increase in length of the fiber. Therefore, for a given fiber, the FBG has to be inscribed in a core closer to the surface of the fiber and the position of the FBG has to be closer to the fixed point.

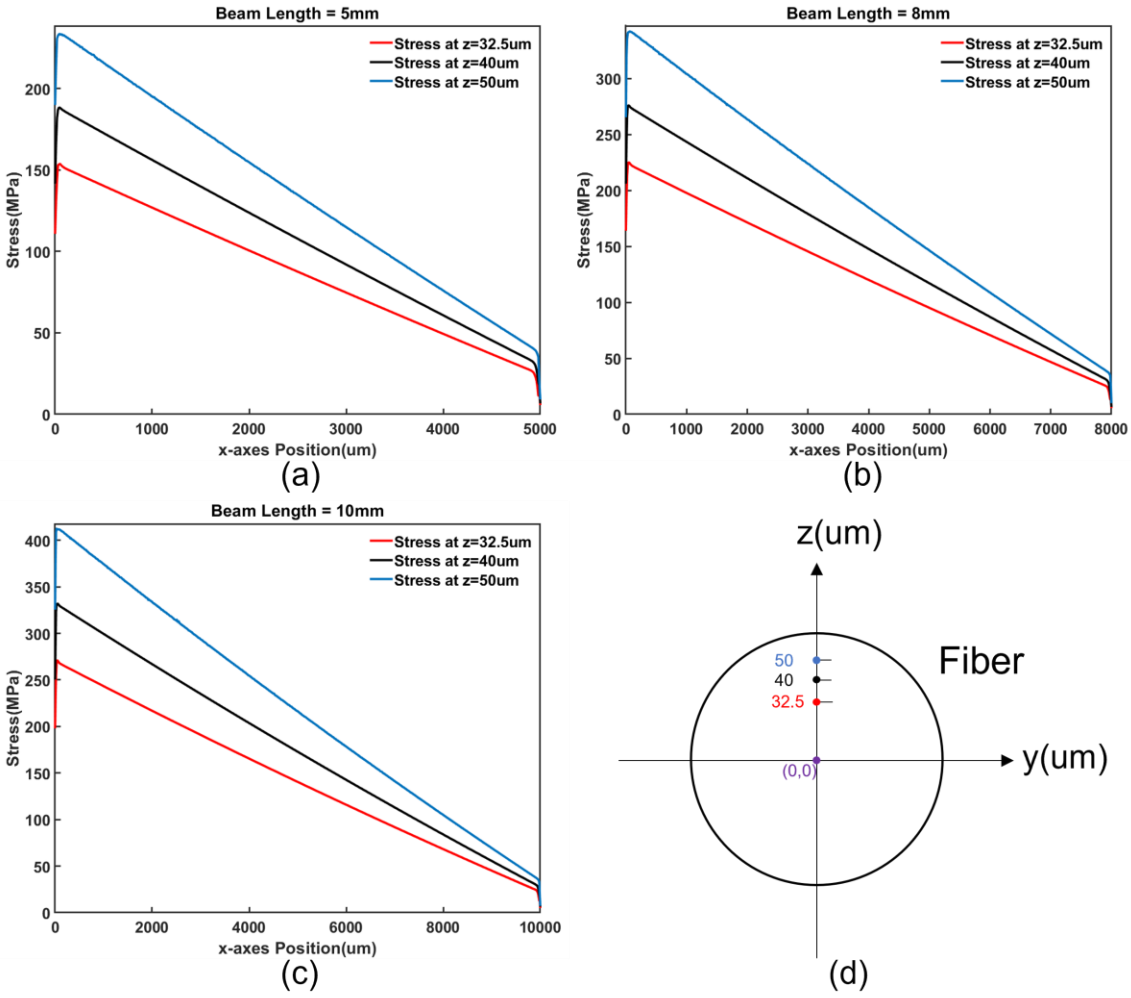

Figure 28. Stress distribution at different values of x for beam with length (a) 5mm (b) 8mm and (c) 10mm. (d)The position of points along Z direction.

The resonance frequency of the cantilever beam structure is also an important factor in the design of accelerometer. Therefore, the variation in eigen frequency (resonance frequency) with beam length is also studied using COMSOL. The resonant frequency (ω_0) of this type of structure can be expressed by equation (3.6) [102]

$$\omega_0 = \sqrt{\frac{3EI}{mL^3}} \tag{3.6}$$

where *m* is mass at the tip and the other terms have their usual meaning that were described in earlier section. As can be seen from Figure 29, the longer beam has a better response for lower frequency regime while the shorter one has better response in higher frequency regime. Therefore, appropriate beam length for a particular frequency range can be considered depending upon the requirement.

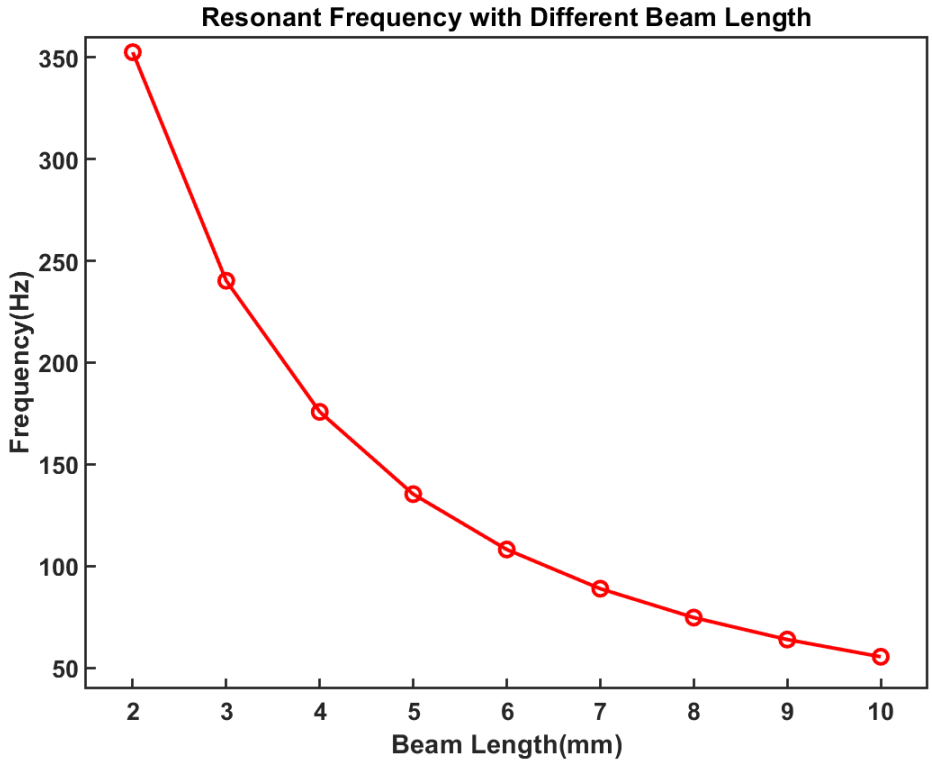

Figure 29. Resonant frequencies for different beam length.

3.2 Dynamic Analysis

In this section, a sinusoidal force is applied to the tip of the cantilever and the resulting stress variation along the length and cross section of the fiber are analyzed. A varying force with maximum amplitude = 0.01N in the form of a cosine wave function $0.01\cos(2\pi ft)$ where $f = 30Hz$ is applied to the cantilever with its length fixed at 10 mm as shown in Figure 30. Three positions along the length of fiber beam and three positions along the cross-section were selected for evaluation of stress as shown in Figure 31 (a) and (b) respectively. The stress variation corresponding to x=1mm, 4mm and 7mm are shown as Figure 32 (a) and (b), respectively. The results show that stress is stronger at positions close to the fixing point along the length of fiber and far from center of fiber along the cross section. Therefore, the response is similar to that in case of static applied force.

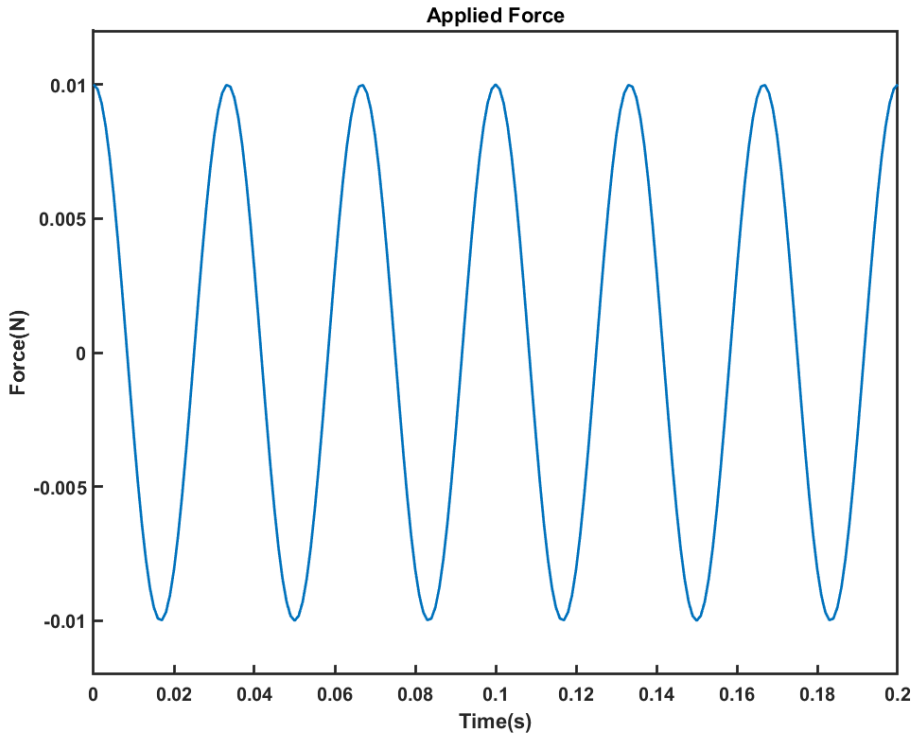

Figure 30. Time variation of applied force (cosine wave)

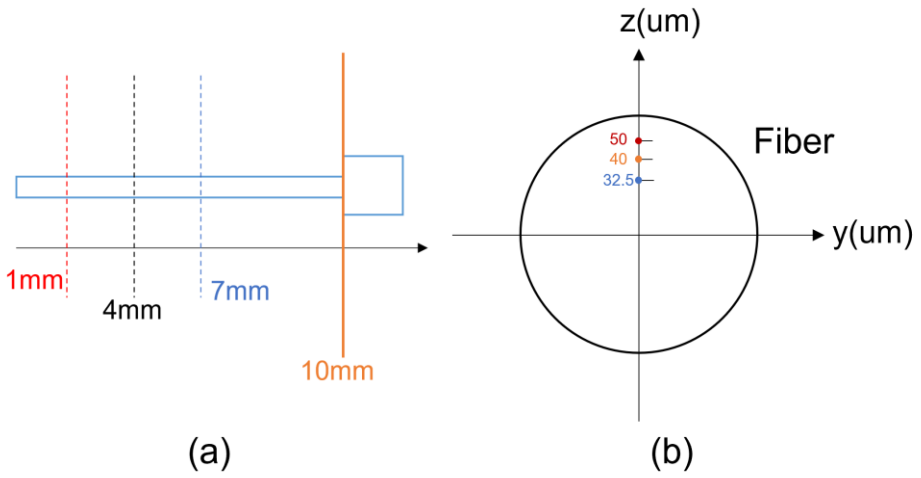

Figure 31. (a) Selected points along the fiber beam. (b) Selected points along the cross-section of fiber.

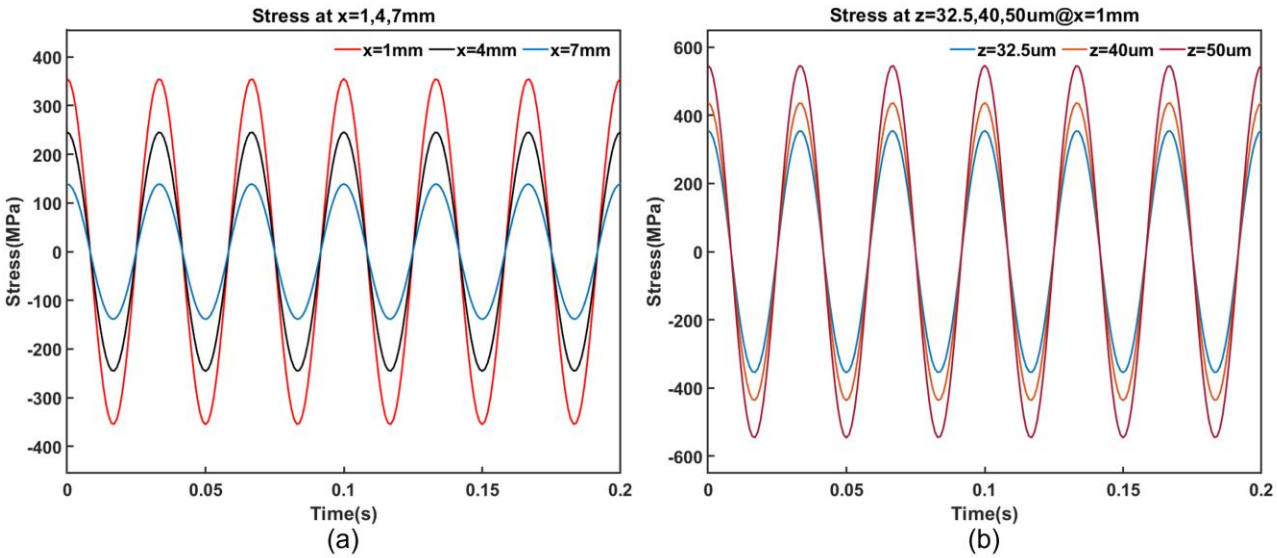

Figure 32. (a) Variation of stress with time at x=1(red), 4(black), 7(blue)mm, (b) Variation of stress with time at z=32.5(blue), 40(orange) and 50(brown)um with x=1mm

3.3 Multicore Fiber For 1-Axis Vibration Measurement

In this section, a homemade fiber with three cores was used to validate the simulation results. The microscopy image of three-core fiber (TCF) is shown as Figure 33 (a). All the cores were located at a distance of z=32.5 μm from the center of the fiber. In order to study the effect of fiber length on the response of the cores to applied vibration, three probes (i.e. fiber beams) with length 5mm, 8.2mm and 11mm were considered for experimental investigation. First, one of the cores of TCF was

inscribed with FBG (length=1 mm) using fs laser based PbP technique. The TCF was spliced with a section of SMF by aligning the core with inscribed grating with the core of SMF. Thereafter a mass of 15 mg was attached to the tip of the TCF and the other end of the probe was connected to an interrogator to monitor the FBG spectrum. The cantilever system consisting of the TCF with mass attached at tip was fixed on a rotator which in turn was fixed on a shaker to provide necessary vibration. The fiber is rotated along its axis and at each orientation, the response of the FBG spectrum to the applied vibration was monitored and consequently, the fiber was fixed at an orientation that corresponds to maximum sensitivity. The position of the cores for maximum sensitivity is shown in the schematics in Figure 33 (b).

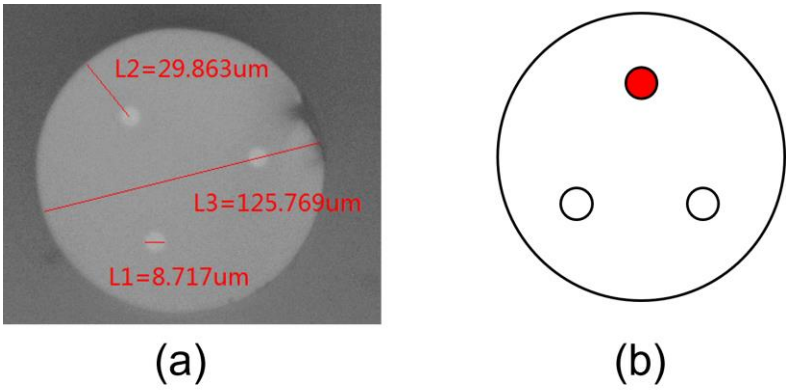

Figure 33. (a) Microscopic image of TCF. and (b) The schematic of position of core inscribed with FBG for maximum response to applied vibration.

The spectra of the FBGs corresponding to the three samples of TCF (length=5mm, 8.2mm and 11mm) are shown in Figure 34 (a-c), respectively and their corresponding 3dB bandwidth are 0.88nm, 1.06nm and 1.05nm. The experimental set up for vibration measurement is shown in Figure 35. The TCF was fixed on a rotator with the FBG being very close to the fixed point. The response of these probes to applied vibration was investigated by monitoring the shift in peak wavelength of FBG using an interrogator (Micron Optics HYPERION si255) with sampling frequency of 5 KHz.

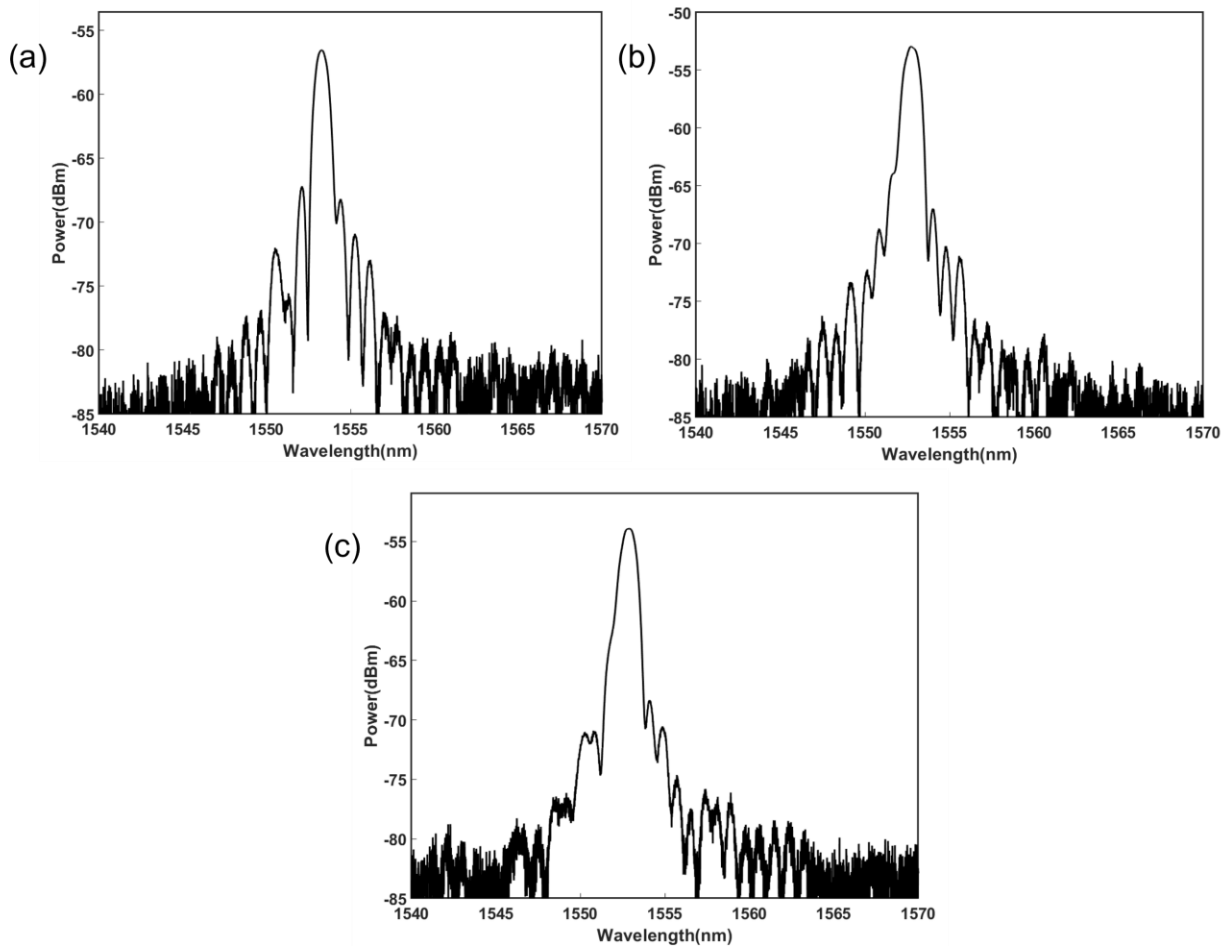

Figure 34. FBG spectrum written in fiber with (a)5mm (b)8.2mm (c)11mm beam length.

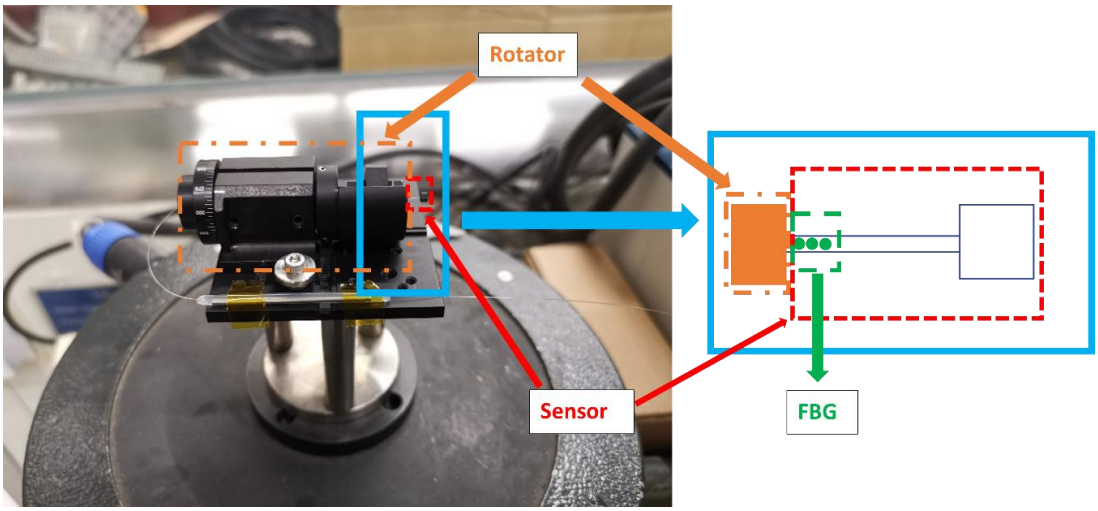

Figure 35. Experimental set up for vibration measurement

The frequency responses of all these probes are shown as Figure 36.

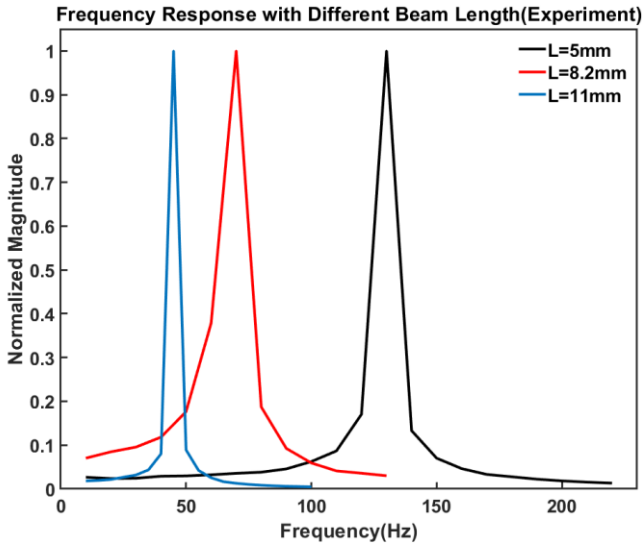

Figure 36. Frequency response of the cantilever structure for different beam lengths: 5mm(Black), 8.2mm(Red), 11mm(Blue)

As can be seen from the figure, the resonant frequency of probes with length 5mm, 8.2mm and 11mm are around 130Hz, 70Hz and 45Hz respectively. The corresponding simulated frequency response of all these probes are found to be 136Hz, 72Hz and 48Hz respectively as shown in Figure 37(a). The comparison of simulation and experimental results are shown as Figure 37(b) which shows that the experimental results are in good agreement with the simulated results. The vibration sensitivity of these probes was investigated at a frequency far below the corresponding resonance frequency. For instance, the vibration response of probe with length 5 mm and resonance frequency 130 Hz were investigated at 80 Hz. Similarly, for other two probes with resonance frequency of 70 Hz and 45 Hz, the response was investigated at 30 Hz and 25 Hz respectively. The shift in peak wavelength of the FBG in each probe to applied acceleration varying from 0.5 g to 3 g (upward) was recorded and thereafter the response was recorded for acceleration varying from 3 g to 0.5 g (downward). The response of all these probes to applied acceleration is shown in Figure 38 (a), (b), and (c) respectively and the results are summarized in Table 2. The results show that for a given position of FBG, the

acceleration sensitivity increases with increase in length of the probe. Furthermore, it can be seen that the response of these probes to applied acceleration is nearly similar for both orientation (upward and downward) of core of the TCF.

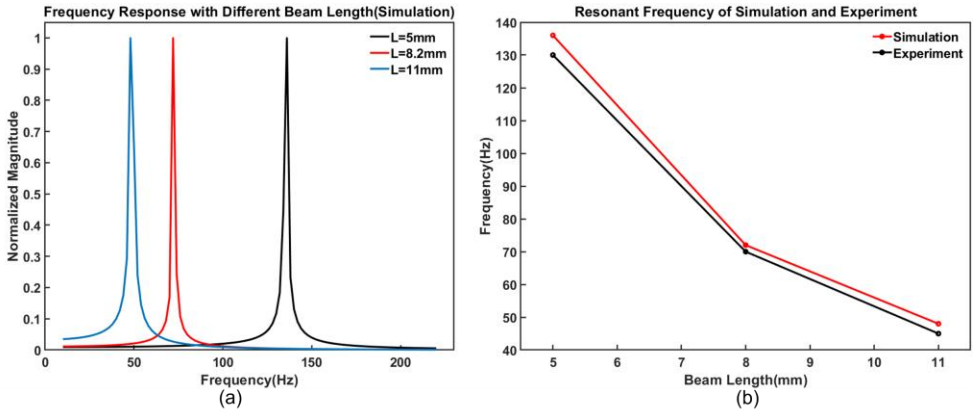

Figure 37. (a) Simulated frequency response for different beam lengths: 5mm(Black), 8.2mm(Red), 11mm(Blue) (b) Comparison of simulated and experimentally obtained resonance frequencies Simulation(Red), Experiment(Black).

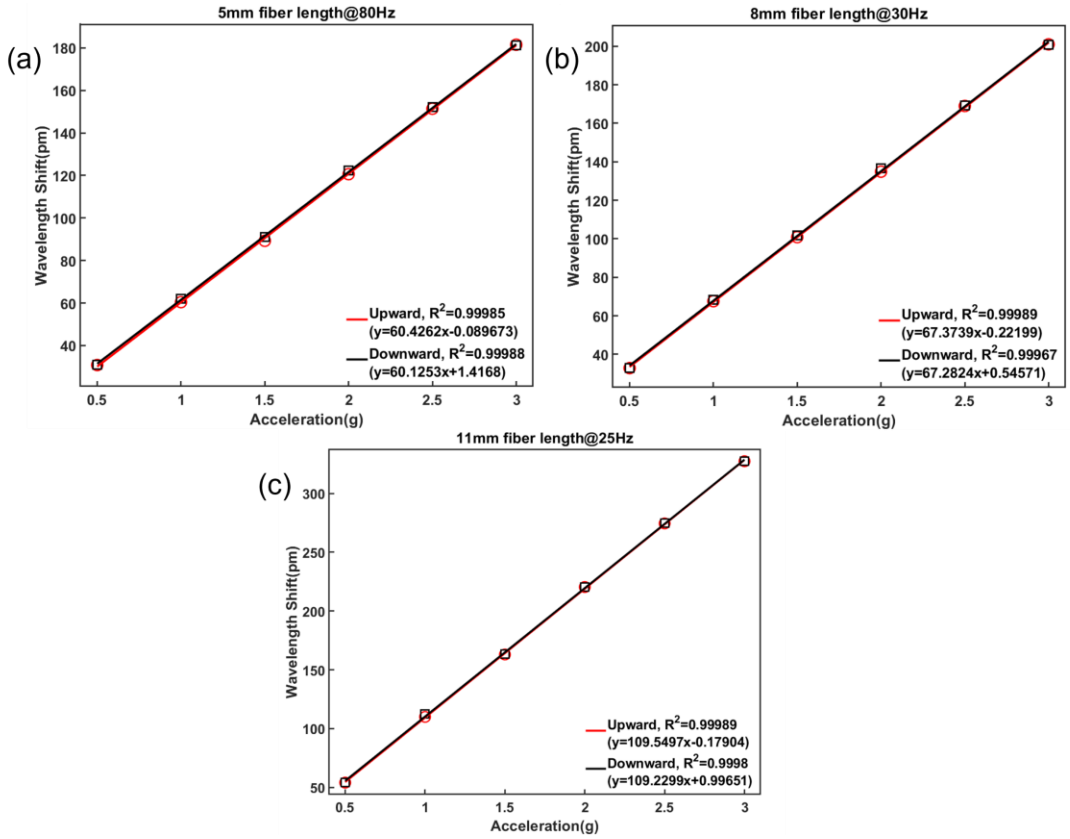

Figure 38. Sensitivity of sensor with different beam lengths: (a) 5mm, (b) 8.2mm, (c) 11mm

Table 2. Sensitivity of the sensors for increasing and decreasing accelerations.

Beam Length	Measured Frequency	Increasing Acceleration (0.5g to 3g)	Decreasing Acceleration (3g to 0.5g)
5mm	80Hz	60.4pm/g	60.1pm/g
8.2mm	30Hz	67.37pm/g	67.28pm/g
11mm	25Hz	109.5pm/g	109.22pm/g

The investigation of variation in length of probe on acceleration sensitivity was followed by the analysis of acceleration sensitivity for different positions of FBG along the length of the fiber. The length of the probe was fixed at 10 mm and three FBGs at a distance of 0.75 mm, 4.25 mm, and 7.75 mm from the fixed position were inscribed along the length of the fiber as shown in Figure 39. The resulting spectrum corresponding to three FBGs is shown in Figure 40.

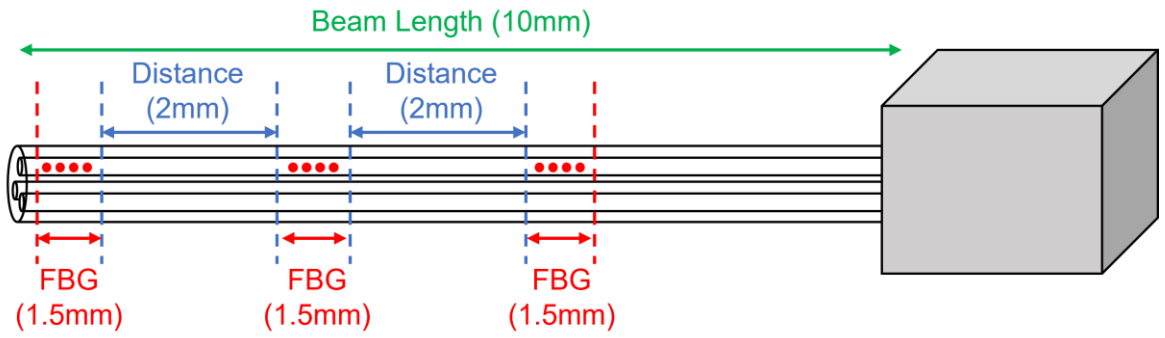

Figure 39. FBGs at different positions along the fiber.

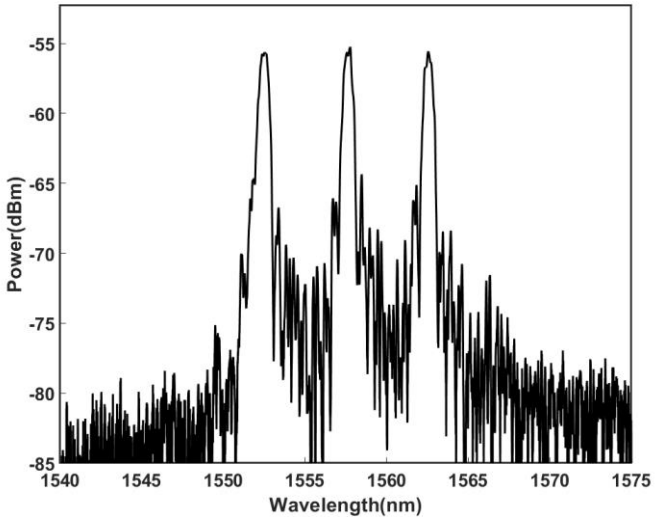

Figure 40. Spectrum of three FBGs.

The response of all FBGs were recorded at a fixed resonance frequency of 30 Hz. The resulting shift in peak wavelength of FBG to at applied acceleration of 1g is illustrated in Figure 41. As can be seen from the figure, the wavelength shift is maximum for FBG closer to the fixed position, and it decreases as we move towards the tip of the probe and this trend agrees well with the simulation results obtained in previous section. The corresponding acceleration sensitivity of all these FBGs are summarized in Table 3.

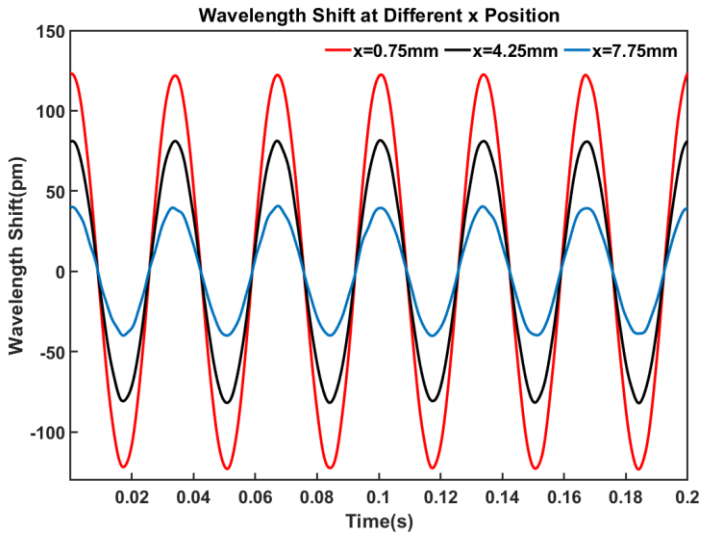

Figure 41. Response of three FBGs for different x positions.

Table 3. Acceleration sensitivity at different positions of x along the fiber length.

Position	Sensitivity
x=0.75mm	121.9pm/g
x=4.25mm	81.07pm/g
x=7.75mm	40.71pm/g

3.4 Summary

In this chapter, stress distribution in optical fiber-based cantilever beam structure was analyzed using FEM based software. The beam was subjected to both static and dynamic force and the stress distribution along the length as well as the cross section of the fiber was investigated. The analysis showed that longer beam has higher stress at a given position along the length of optical fiber. Furthermore, stress is higher at positions close to the fixing point for a given fiber length. On the other hand, in a given cross sectional plane, the stress was found to be stronger at the positions that were far from the neutral axis. The length of the beam was also found to affect the resonance frequency and depending upon operational requirement, it could be tuned. The simulation results were validated by using a TCF based cantilever beam for vibration analysis. All the experimental results agreed well with the simulation results. However, the TCF could be used for vibration analysis along one axis only because of the non-availability of coupler for three cores of the homemade TCF. Therefore, in the next chapter, a multicore fiber along with a commercial coupler will be used to make an accelerometer that can be used for multi-axis measurement.

Chapter 4. Two-axis Compact and Lightweight Accelerometer Design

In this chapter, the design and fabrication of a two-axis accelerometer based on multicore fiber has been carried out. A detailed process to inscribe FBGs in two of the seven cores of MCF using femtosecond laser based PbP technique has been presented. Simulations have been carried out to find optimized position of FBGs for maximum response to applied acceleration at a proper operational frequency. The packaging of the sensor in a compact aluminum box and the subsequent response of the system to applied acceleration under different conditions have been presented.

4.1 Sensor Fabrication

Prior to the fabrication process of the cantilever beam-based sensor, factors such as stress distribution and frequency response of the sensor were optimized as per the application requirement using FEM-based simulation software (COMSOL Multiphysics). A section of silica fiber together with an attached nickel mass were considered as the combined sensing body. The fiber was fixed at one end with the mass attached to the other end. The parameters of different components that the sensing body comprises of are listed in Table 4.

Table 4. Parameters of Sensor Components

Material	Diameter (mm)	Length (mm)	Density (kg/m^3)	Young's Modulus (GPa)
Silica (Fiber Beam)	0.15	8	2200	70
Acrylic (Coating)	0.25	8	1190	3.2
Nickel (Proof Mass)	1.7	2	8900	200

The simulation process was carried out using the mechanical module available in COMSOL Multiphysics software. The resulting stress distribution along the sensing body without and with an applied force of 3.8mN (corresponding to the maximum displacement at 40Hz) are shown in Figure 42 (a) and (b). As can be seen from the figure, the stress is maximum near the fixed position, and it decreases gradually along the fiber direction to the other side. The reason for this response can be explained by equation (3.4).

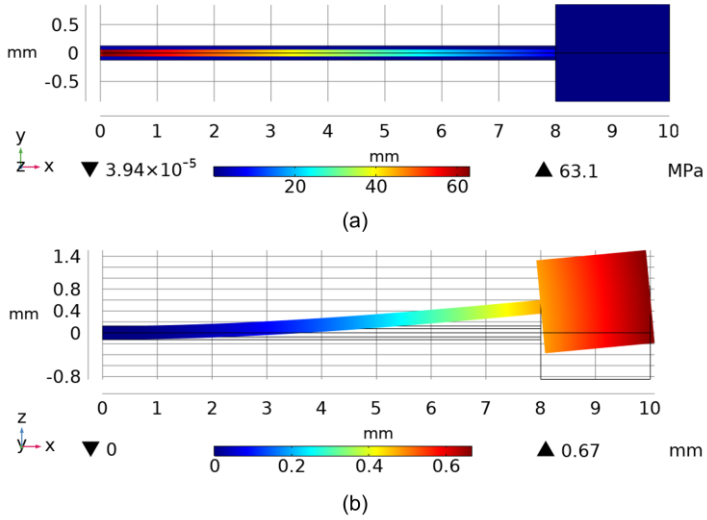

Figure 42. (a) Stress distribution along the cantilever beam structure at 0 Hz and (b) with maximum displacement under 40Hz oscillation.

In order to have an optimum response, the grating should be inscribed as close as possible to the fixed position and the length of the grating should be confined to the position corresponding to the maximum stress region. Furthermore, the frequency response of the sensor was also simulated, and a resonant frequency was found to be around 76 Hz. The operational frequency of the accelerometer as per the EN50317 standard for current collection system of the dynamic interaction between pantograph and overhead contact wire varies from 0-20 Hz [103,104]. Therefore, the parameters listed in Table 4 are suitable for the fabrication of the required sensor. However, it should be noted that during practical implementation, there will be

around 10% tolerance of these parameters resulting in a slight shift in the resonance frequency.

The fabrication process of the cantilever-based accelerometer involved the inscription of FBGs in a section of seven-core MCF (YOFC, Core-to-core (adjacent) distance=41.5±1.5μm) and the attachment of a nickel-based hollow cylindrical mass onto the fiber tip. The diameters of the core and cladding of the MCF were ~8 μm and ~150 μm, respectively while the pitch of the cores was 42 μm as shown in Figure 43 (a). A femtosecond laser (Spectra-Physic, SpOne-8-SHG) centered at 520 nm and with a pulse duration of 250 fs was used to inscribe FBGs in two cores of the MCF by means of point-by-point technique. The average power of the laser was around 12.5μW and the laser beam was focused onto the cores using a microscopic objective lens (×40 magnification and NA= 0.75). Two individual cores such as core 2 and core 3 in Figure 43 (b) were chosen to inscribe FBGs without removing the coating. The speed of the translational stage was fixed at 160 μm/s and 160.5 μm/s for core 2 and core 3, respectively while the length of each grating was 1 mm. The resulting FBG spectra corresponding to these cores are shown in Figure 43 (c). Afterward, a nickel tube with length, outer diameter, weight, and inner diameter of 2 mm, 1.7 mm, 38 mg, and 0.3 mm, respectively was glued to the fiber tip. The inner diameter of the tube matches well with the coating diameter of ~0.25 mm, with the schematic presented in Figure 44. The structural symmetry of the mass ensures uniform vibration characteristics in all orientations. The structural symmetry of the mass ensures uniform vibration characteristics in all orientations. Thereafter, the sensing probe was fixed inside an aluminum alloy box using glue (LOCTITE 431) where the dimensions of the box were 23 mm × 10 mm × 10 mm as shown in Figure 45. The total weight of the box along with the 2-axis sensor was 5.2 grams weighing less than the commercial optical 1-axis accelerometers such as Micron Optics os7100

(weight = 28 grams and 2-axis measurement requires a fixture to assemble 2 accelerometers with total weight > 56 grams). It should be noted that the lengths of the FBGs were fixed at 1 mm to ensure better sensitivity since the stress was maximum within 1.5 mm from the fixed position as shown in Figure 42. As per the simulation results, the distance between the fixed position and gratings should be zero. However, due to the installation limitation, experimentally, this distance was detected to be around 1 mm. The response of the sensor to different applied accelerations was investigated with and without the presence of damping oil (viscosity = 1000 cst) inside the box. Figure 46 (a) and (b) show the packaged sensor and orientational illustration after the installation of the sensing probe respectively.

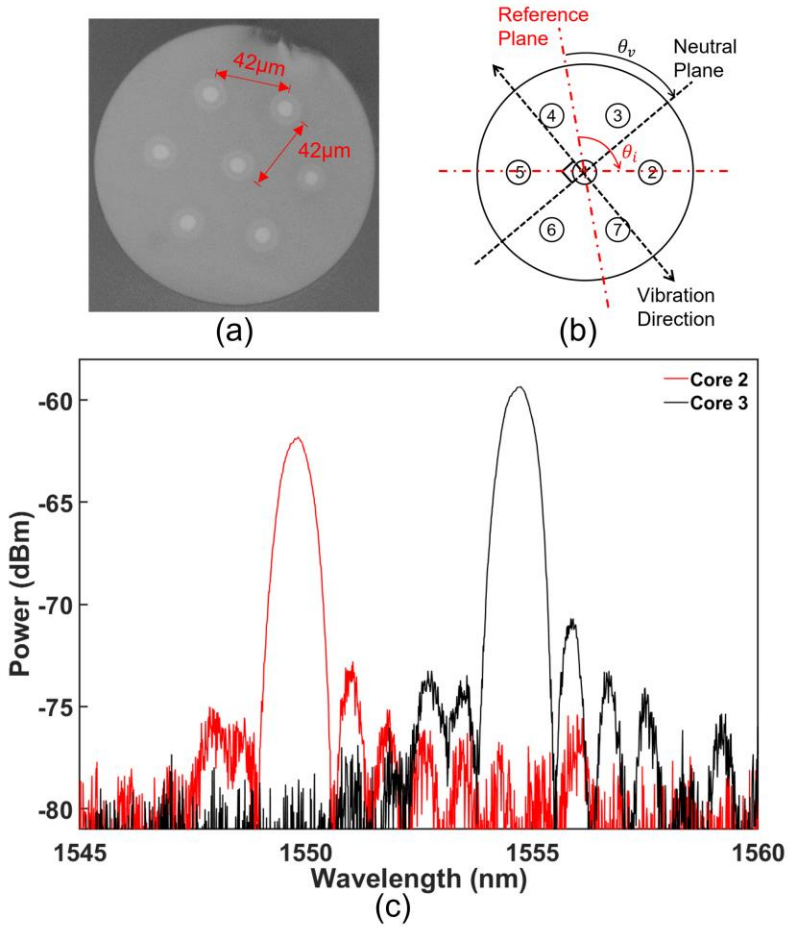

Figure 43. (a) The microscopic image, (b) schematic of cross-section and (c) the FBG spectra corresponding to core 2 (red) and core 3 (black) of the MCF respectively.

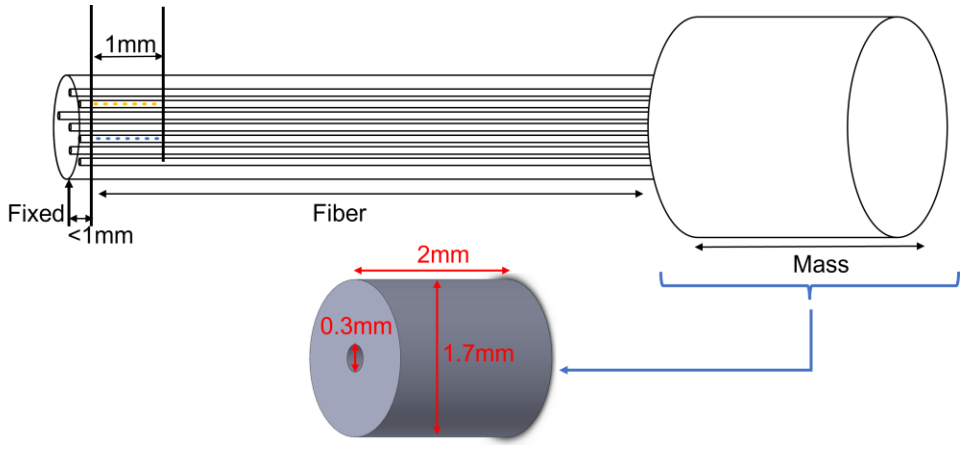

Figure 44. Schematic of the cantilever beam structure. The inset shows the schematic of the cylindrical mass with its dimensions.

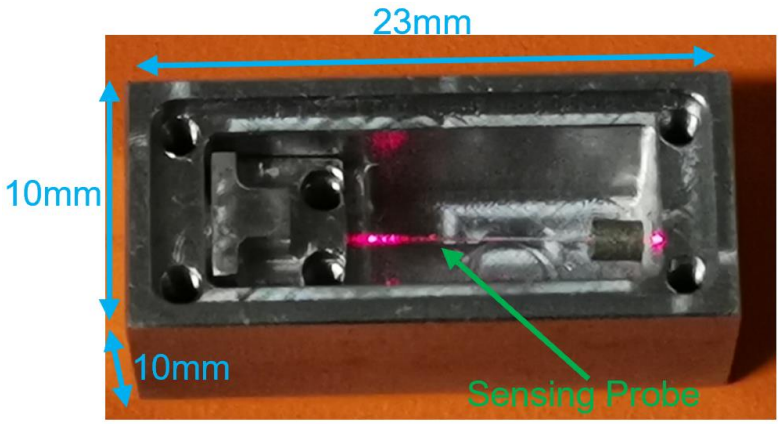

Figure 45. The packaged sensor

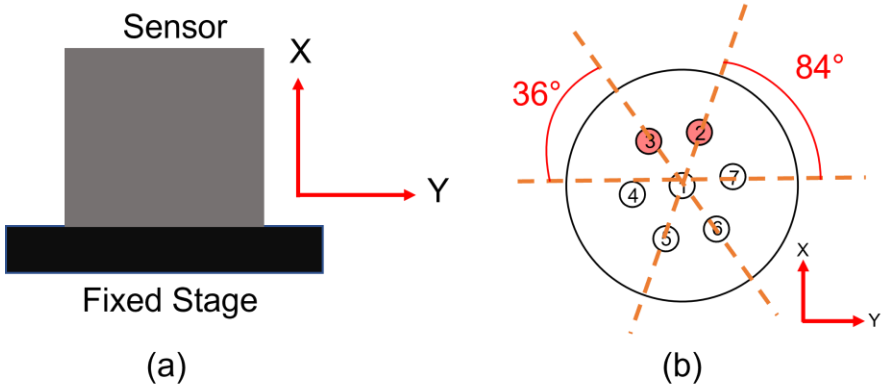

Figure 46. (a) Packaged sensor fixed on the shaker. (b) Fiber core orientation after packaging (Not to scale)

4.2 Experiment Setup

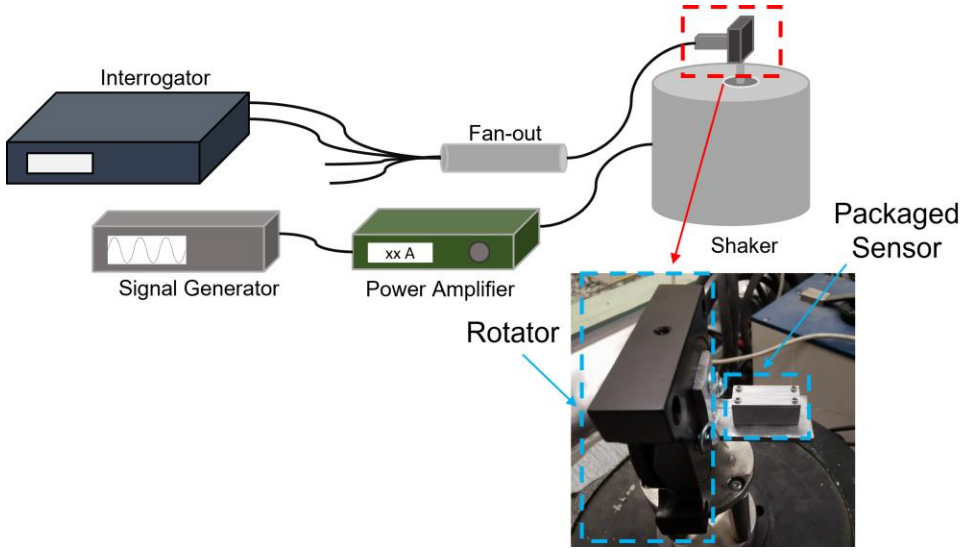

Figure 47. Experimental setup for acceleration measurement

The experimental setup is depicted in Figure 47. Firstly, the packaged sensor was fixed onto a rotational stage and the rotational stage was mounted on a shaker (Bruel&Kjaer 4808). A signal generator connected to a power amplifier drives the shaker that aids in introducing a sinusoidal vibration of the sensor thereby providing the necessary acceleration. The corresponding wavelength shifts of FBGs due to the applied acceleration were monitored by an interrogator (Micron Optics HYPERION si255, wavelength accuracy=2 pm) with 5 kHz sampling rate. All these measurements were carried out at frequencies lower than the resonance frequency. The schematic of the neutral plane and the vibrational direction of the sensor are shown in Figure 43 (b). The θ_v = 0° was defined as the position where reference plane aligns with the neutral plane as shown in Figure 43 (b), θ_i (i=1, 2, 3…) was the angle between the fiber core and reference plane where the reference plane was randomly defined and aligned with the center of the fiber. In this case, the reference plane was aligned with core 2 (θ_2=0°). The orientation of the fiber was adjusted from 0° to 180° in steps of 10°. The vibration orientations were reconstructed using the following equation (4.1) [96,105,106]

$$\theta_v = \tan^{-1}\left(\frac{\frac{\Delta\lambda_2}{\lambda_2}\sin(\theta_3) - \frac{\Delta\lambda_3}{\lambda_3}\sin(\theta_2)}{\frac{\Delta\lambda_3}{\lambda_3}\cos(\theta_2) - \frac{\Delta\lambda_2}{\lambda_2}\cos(\theta_3)}\right) \quad (4.1)$$

where θ_2=0°, θ_3=60°. λ_2 and λ_3 refer to the central wavelength of FBGs in core 2 and core 3 whereas $\Delta\lambda_2$ and $\Delta\lambda_3$ refer to the wavelength shift in core 2 and core 3 respectively.

The sensitivity of x-axis and y-axis of sensor was tested and defined as Figure 48. The sensitivity of x-axis was measured on x direction vibration (Figure. 48 (a)) while the sensitivity of y-axis was measured on y direction vibration (Figure. 48 (b)).

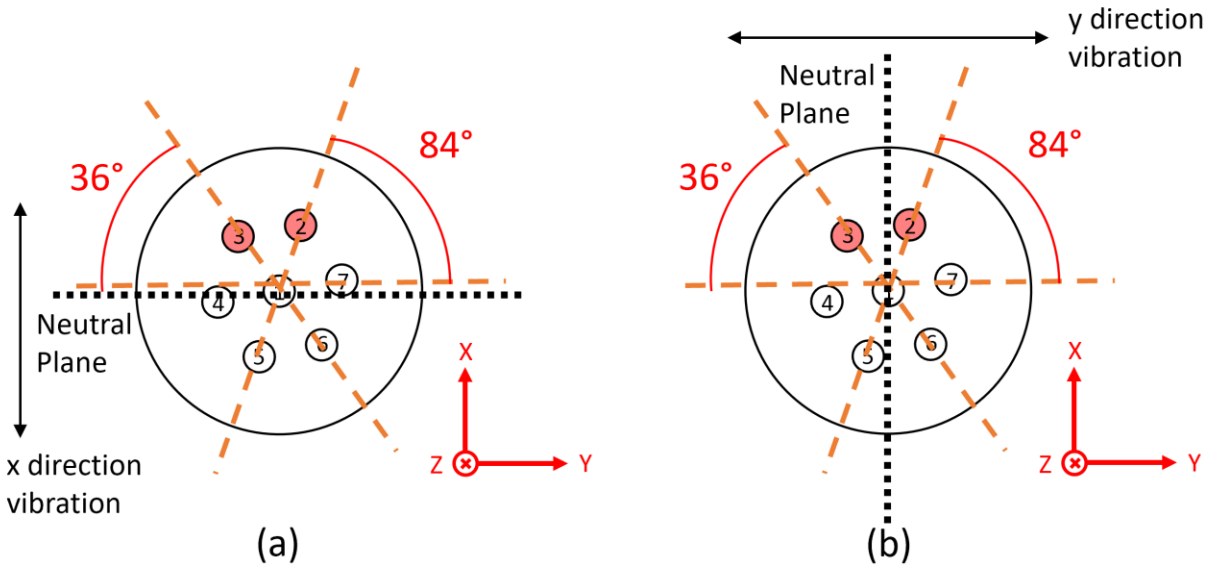

Figure 48. Sensitivity measurement of (a) x-axis and (b) y-axis

4.3 Experiment Results

Initially, the response of the sensor was investigated without the use of damping oil. The resonance frequency of the sensing probe was determined by plotting the vibration amplitude against the applied frequency ranging from 10 Hz to 110 Hz as shown in Figure 49. As can be seen from the figure, the resonance frequency was found to be 75 Hz (black line), which exhibits a good correlation with the simulation

results (red line). The difference of bandwidth between experiment and simulation is attributed to the different scanning steps (5Hz in experiment and 2Hz in simulation).

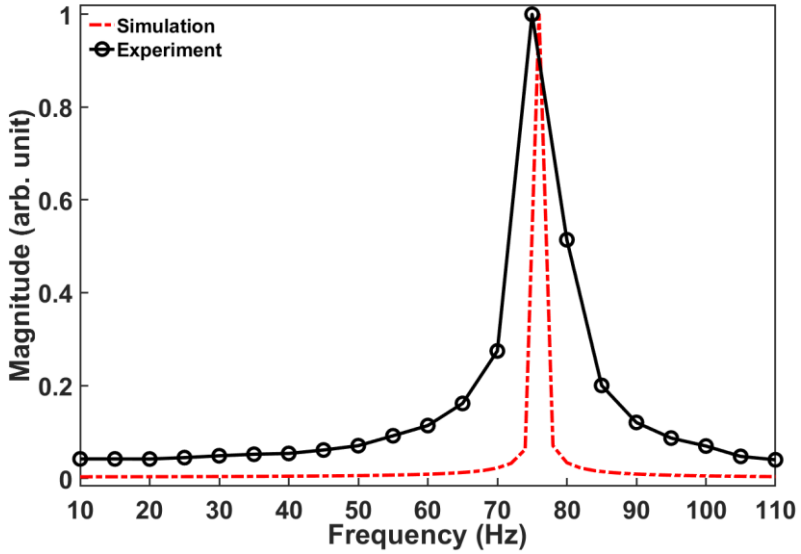

Figure 49. Frequency response of the sensor

Next, the response of the FBGs to the applied acceleration (1 g to 5 g, limited by the inner dimension of box) was investigated under different θ_v while keeping the input frequency fixed at 40 Hz. The response of the sensor along two vertical directions (X and Y) with the absence of damping oil is shown in Figure 50 (a) and (b) respectively. As can be seen from Figure 50 (a) and (b), the acceleration sensitivities of core 2 and core 3 along the X-axis are ~85 pm/g (tolerance≈6 pm) and ~63 pm/g (tolerance≈3 pm), respectively while the same along the Y-axis are ~14 pm/g (tolerance≈1 pm) and ~77 pm/g (tolerance≈3 pm), respectively. The different sensitivities along the X- and Y- axes can be attributed to the different orientations of core 2 (~84° with respect to the X-axis) and core 3 (~36° with respect to the X-axis) (see Figure 46 (b)). Afterwards, this measurement was repeated for different orientation angles and the orientation-dependent sensitivity is plotted in Figure 51. As can be seen from the figure, there is a 60° phase shift between core 2 and core 3

which can be attributed to the angular difference between the two cores. The difference in sensitivity of both cores may be attributed to the difference in position of FBG in core 2 and core 3 with respect to center of the fiber.

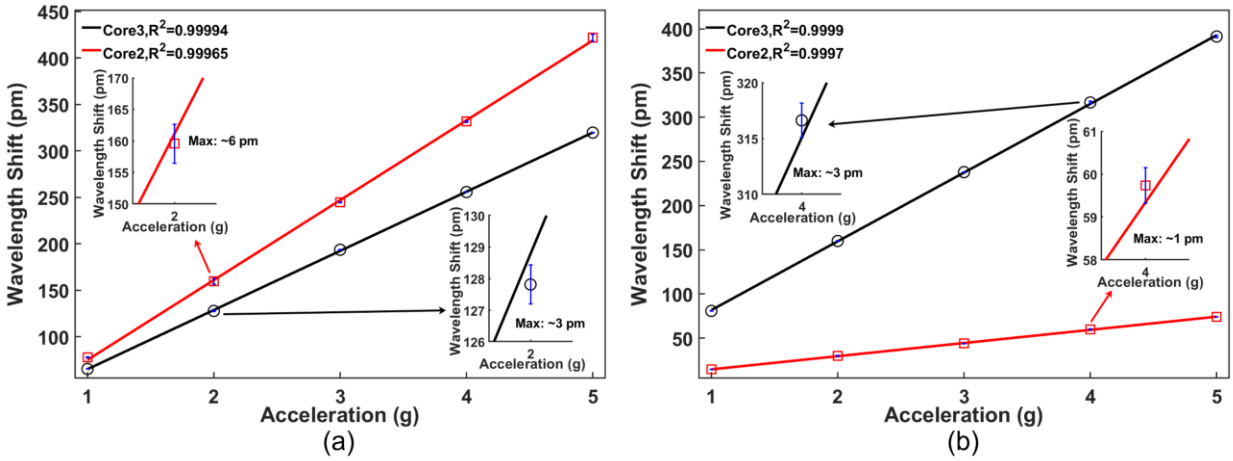

Figure 50. Response of the sensor to applied acceleration along (a) x-axis (θv=84°) and (b) y-axis in the absence of damping oil. (θv=174°, f=40Hz).

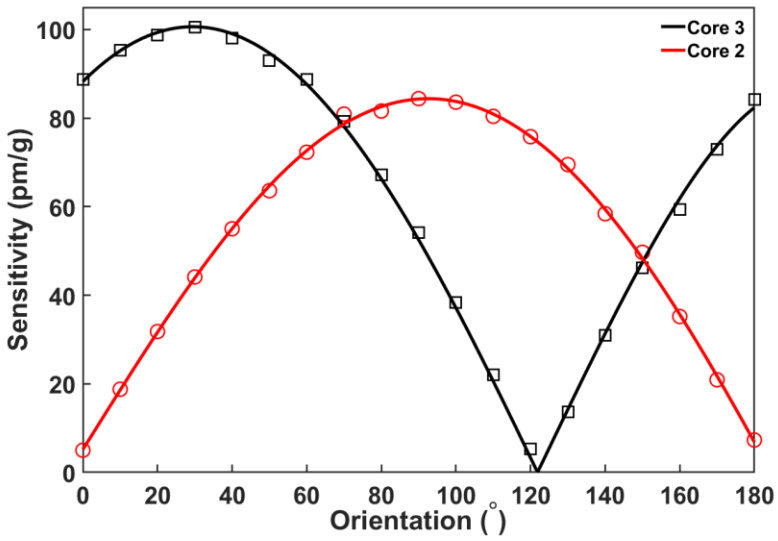

Figure 51. Orientation-dependent sensitivity

The above investigations for acceleration measurements were repeated by filling the box with damping oil to protect the accelerometer from high impact, for railway applications. The viscosity of damping oil was 1000 cst and the response of the probe was investigated for applied acceleration from 1 g to 10 g at which point the response

of the corresponding cores reduced. The acceleration sensitivities of core 2 and core 3 along the X-axis are ~18 pm/g (tolerance≈1 pm) and ~14 pm/g (tolerance≈1.5 pm), respectively while the same along the Y-axis are ~3.4 pm/g (tolerance≈0.5 pm) and ~19 pm/g (tolerance≈0.3 pm), respectively as can be seen from Figure 52 (a) and (b) respectively. Therefore, even in the presence of damping oil, the maximum response of the cores (18 pm/g and 19 pm/g) were found to be adequate for practical applications.

Additionally, the orientation-dependent sensitivity of the packaged sensor with the oil-damped accelerometer is shown in Figure 53. As can be seen from Figure 53 (a), the response of the sensor after filling of damping oil follows the same trend as that before the filling of damping oil (see Figure 51). The input orientation angles with respect to the reconstructed orientation angles (θ_v) based on equation (4.1) are plotted in Figure 53 (b) along with errors in the inset and both the results perfectly match each other with an R^2 value of 0.9994. The error of ±5° can be attributed to factors such as manual mechanical control of the rotator, and the difference in sensitivity of core 2 and core 3 as well as the geometry error caused by manual packaging process.

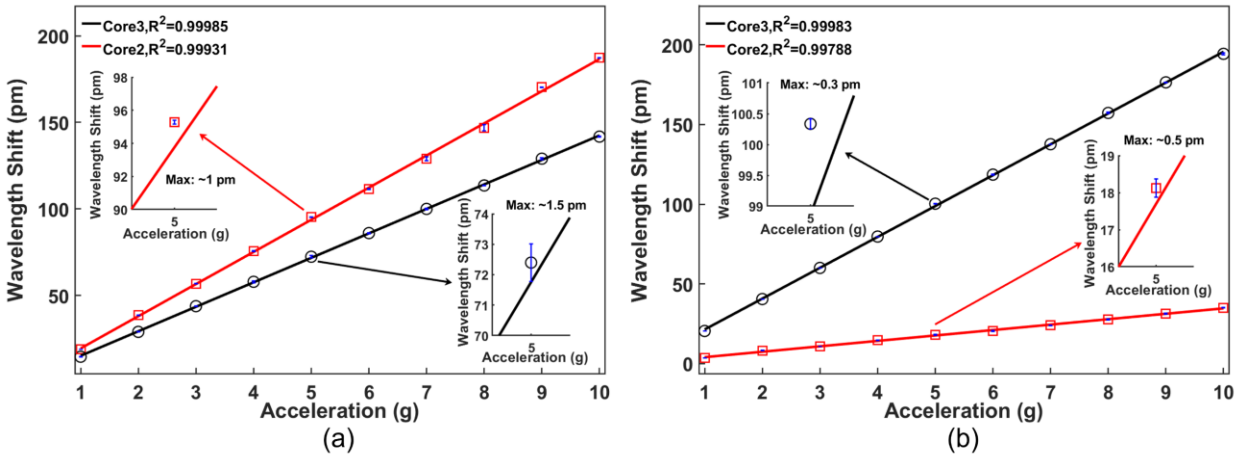

Figure 52. Response of the sensor to applied acceleration along (a) x-axis (θv=84°) and (b) y-axis in the presence of damping oil. (θv=174°, f=40Hz).

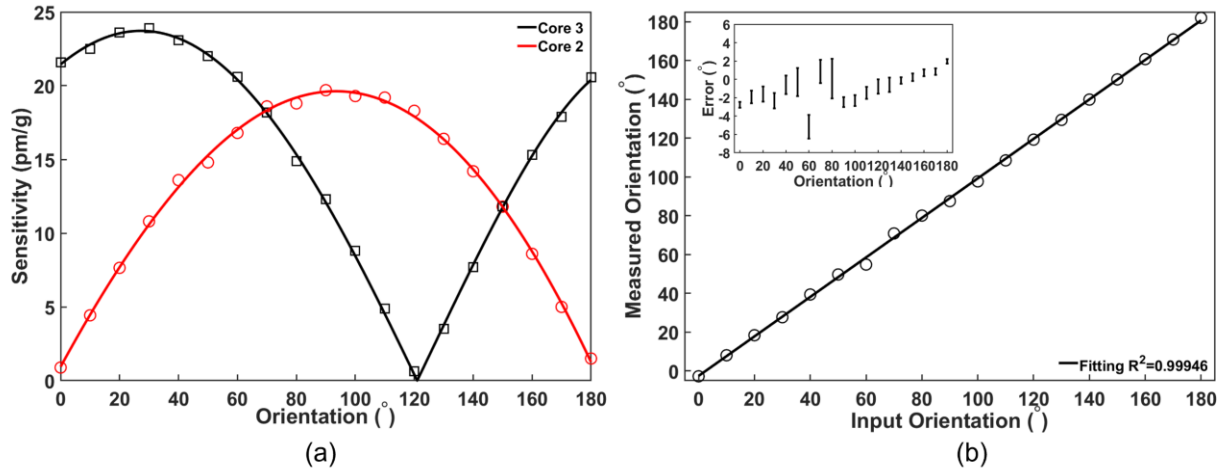

Figure 53. Orientation-dependent sensitivity of packaged sensor with damping oil and (b) the reconstructed orientation angles with errors (inset).

Furthermore, the frequency response of the sensor was also affected in presence of the damping oil. The response of the sensor in the frequency range of 10 Hz to 110 Hz with the filling of damping oil is shown in Figure 54. As can be seen in Figure 54, the bandwidth of the frequency response curve in the presence of damping oil is around 25 Hz. Additionally, the response of the packaged sensor to survive high impact up to 25 g was also investigated to ensure its robustness. The acceleration was increased from 10 g to 25 g and the wavelength shift of the FBG peak corresponding to core 3 is shown in Figure 55.

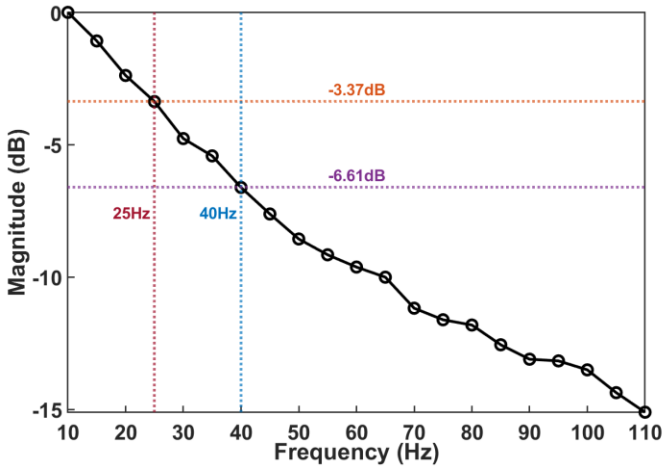

Figure 54. Frequency response of packaged sensor with damping oil.

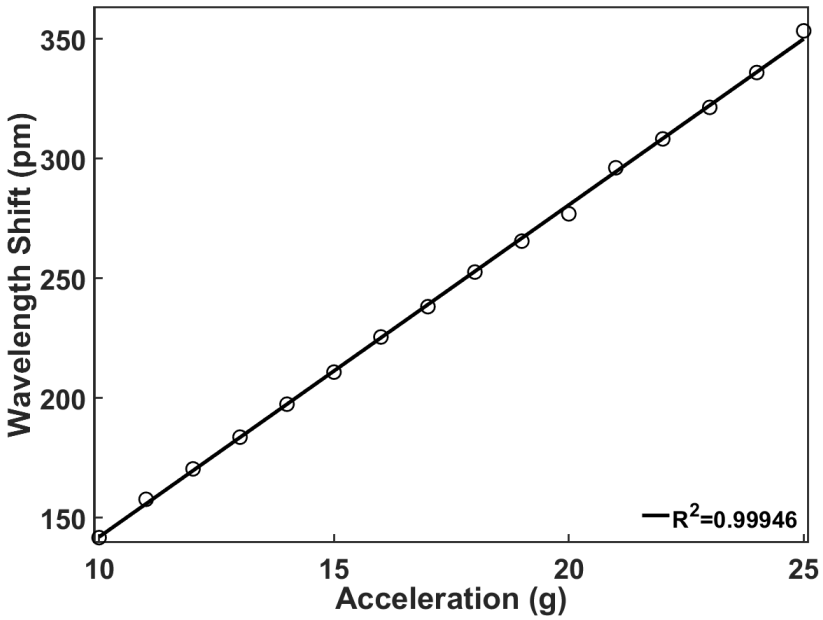

Figure 55. Response of the sensing system to higher accelerations from 10 g to 25 g.

As can be seen from the figure, the response is linear with a sensitivity of 14 pm/g. It should be noted that the maximum acceleration investigated using the current experimental setup is limited by the power amplifier (which is used to drive the shaker).

4.4 Summary

In this chapter, a cantilever beam-based two-axis accelerometer using an FBG-inscribed MCF has been proposed for pantograph-catenary system monitoring. Two well-distinguishable FBGs have been inscribed in two of the seven cores in MCF using a femtosecond laser without removing the coating of the fiber thereby making it a robust probe. Furthermore, the use of multicore fiber led to the measurements of acceleration at different orientations. The probe was packaged in a compact box for practical implementation with a total weight of the system amounting to just 5.2 grams, which weighs less than 10% of commercial FBG-based accelerometers. The response of the system to the applied accelerations in orientations ranging from 0 to 180° has been investigated in air as well as with the packaging box filled with

damping oil. The maximum acceleration sensitivity of the probe in air and oil were 85 pm/g and 18 pm/g, respectively. Additionally, the response of the system to higher values of accelerations has also been investigated in order to ensure its robustness. Hence, the proposed compact lightweight accelerometer can be suitably used for health monitoring of the pantographic system with minimum effect on the dynamic interaction between the pantograph and the contact line.

Chapter 5. Conclusion and Future works

5.1 Conclusion

In this thesis, the design and fabrication of a lightweight optical fiber-based cantilever system has been explored for 2-axis acceleration measurement that can be utilized for pantograph-catenary interaction monitoring system. First, the parameters of the cantilever system of the system have been optimized using FEM based numerical analysis. The stress distribution along the length as well as cross section of the optical fiber has been simulated to achieve maximum response to applied acceleration while the effect of length of the beam on resonance frequency of the system has been simulated to get the desired operational frequency regime. In order to validate the simulation results, one of the cores of a three-core fiber has been inscribed with FBG and the response of this system to applied acceleration has been investigated. The experimental results have been found to be in agreement with those obtained from simulation. Thereafter, a compact and robust two-axis accelerometer based on a multicore fiber has been proposed for pantograph-catenary system. The geometrical parameters of the sensor have been optimized using simulation technique to get maximum response in the desired operational frequency regime. Two of the seven cores of the multicore fiber have been inscribed with well distinguished FBGs using femtosecond laser-based PbP technique without the removal of polymer coating. The sensor has been fixed in a compact aluminum box with the position of FBG being close to the fixed point and the total weight of this packaged sensor has been 5.2 grams which is lighter than some of the commercially available optical accelerometers. After the filling of the box with damping oil, the maximum acceleration sensitivity of one of the cores has been found to be ~18pm/g along X-axis while that of another core has been found to be ~19pm/g along Y-axis for an applied acceleration range up to 10g.Additionally, the deviation in orientation

angle calculated from simulation and experimental data has been found to be small. Furthermore, the robustness of the system has also been investigated by subjecting it to applied acceleration up to 25g.

5.2 Future work

Based on the above investigations, other work can be carried out in future for further improvement in this field.

a) Installing the sensor on pantograph for testing.
b) Improvement in the accuracy of the position of the FBG in the cores of multicore fiber in order reduce the deviation in orientational angle between the theoretical and experimental results.
c) Improvement in accuracy by temperature compensation.
d) Fabrication of a polymer based rectangular shape multicore optical fiber for multi-axis acceleration measurement.

Reference

[1] X. Jin, Z. Wen, W. Zhang, J. Zeng, Z. Zhou Z, Q. Liu. “DEVELOPMENT STATUS OF WORLD RAILWAY AND ITS KEY MECHANICS PROBLEM[J],”. Engineering Mechanics, vol. 20, pp. 90-104, 2004.

[2] S. Bruni, G. Bucca, M. Carnevale, A. Collina, and A. Facchinetti, “Pantograph–catenary interaction: recent achievements and future research challenges,” Int. J. Rail Transp., vol. 6, no. 2, pp. 57–82, 2018.

[3] T. X. Wu and M. J. Brennan, “Basic Analytical Study of Pantograph-catenary System Dynamics,” Veh. Syst. Dyn., vol. 30, no. 6, pp. 443–456, 1998.

[4] W. Zhang, D. Zou, M. Tan, N. Zhou, R. Li, and G. Mei, “Review of pantograph and catenary interaction,” Front. Mech. Eng., vol. 13, no. 2, pp. 311–322, 2018.

[5] T. Koyama, M. Ikeda, S. Kobayashi, K. Nakamura, S. Tabayashi, and M. Niwakawa, “Measurement of the contact force of the pantograph by image processing technology,” Q. Rep. RTRI, vol. 55, no. 2, pp. 73–78, 2014.

[6] P. Boffi et al., "Optical Fiber Sensors to Measure Collector Performance in the Pantograph-Catenary Interaction," in IEEE Sensors Journal, vol. 9, no. 6, pp. 635-640, June 2009.

[7] M. Bocciolone, G. Bucca, A. Collina, and L. Comolli, “An approach to monitor railway pantograph-catenary interaction with fiber optic sensors,” in Fourth European Workshop on Optical Fibre Sensors, 2010.

[8] R. Wagner, D. Maicz, W. Viel, F. Saliger, C. Saliger, R. Horak, T. Noack. “A Fibre Optic Sensor Instrumented Pantograph As Part of a Continuous Structural Health Monitoring System for Railway Overhead Lines,” EWSHM - 7th European Workshop on Structural Health Monitoring, IFFSTTAR, Inria, Université de Nantes, vol. 20, Jul 2014.

[9] M. Tan, N. Zhou, Y. Cheng, J. Wang, W. Zhang, and D. Zou, “A temperature-compensated fiber Bragg grating sensor system based on digital filtering for monitoring the pantograph–catenary contact force,” Proc. Inst. Mech. Eng. Pt. F: J. Rail Rapid Transit, vol. 233, no. 2, pp. 187–200, 2019.

[10] K. Schröder, W. Ecke, M. Kautz, S. Willett, M. Jenzer, and T. Bosselmann, “An approach to continuous on-site monitoring of contact forces in current collectors by a fiber optic sensing system,” Opt. Lasers Eng., vol. 51, no. 2, pp. 172–179, 2013.

[11] M. Bocciolone, L. Comolli, and P. Crosio, “A novel design of a compact S-shaped balance with FBG sensors for the pantograph-catenary contact force measurement,” in OFS2012 22nd International Conference on Optical Fiber Sensors, 2012.

[12] K. Schröder, M. Rothhardt, W. Ecke, U. Richter, A. Sonntag, and H. Bartelt, “Fibre optic sensing system for monitoring of current collectors and overhead contact lines of railways,” J. Sens. Sens. Syst., vol. 6, no. 1, pp. 77–85, 2017.

[13] M. Bocciolone, G. Bucca, A. Collina, and L. Comolli, “Pantograph–catenary monitoring by means of fibre Bragg grating sensors: Results from tests in an underground line,” Mechanical Systems and Signal Processing, vol. 41, no. 1-2, pp. 226–238, 2013.

[14] S. Midya, D. Bormann, T. Schutte and R. Thottappillil, "Pantograph Arcing in Electrified Railways—Mechanism and Influence of Various Parameters—Part I: With DC Traction Power Supply," in IEEE Transactions on Power Delivery, vol. 24, no. 4, pp. 1931-1939, Oct. 2009.

[15] J.-H. Seo et al., “Dynamic analysis of a pantograph–catenary system using absolute nodal coordinates,” Veh. Syst. Dyn., vol. 44, no. 8, pp. 615–630, 2006.

[16] E. L. Iglesias, D. J. Thompson, and M. G. Smith, “Component-based model for aerodynamic noise of high-speed trains,” in Notes on Numerical Fluid Mechanics and Multidisciplinary Design, Berlin, Heidelberg: Springer Berlin Heidelberg, pp. 481–488, 2015.

[17] A. Wilk et al., “Novel method of estimation of inertial and dissipative parameters of a railway pantograph model,” Veh. Syst. Dyn., vol. 60, no. 7, pp. 2413–2435, 2022.

[18] J. Gil, S. Gregori, M. Tur, and F. J. Fuenmayor, “Analytical model of the pantograph–catenary dynamic interaction and comparison with numerical simulations,” Veh. Syst. Dyn., vol. 60, no. 1, pp. 132–155, 2022.

[19] Z. Jian, L. Wenzheng, Y. Meili, and Y. Zhongping, “Simulation analysis of offline characteristics between pantograph and catenary,” IET Electr. Syst. Transp., vol. 7, no. 3, pp. 252–257, 2017.

[20] M. Bocciolone, F. Resta, D. Rocchi, A. Tosi, and A. Collina, “Pantograph aerodynamic effects on the pantograph–catenary interaction,” Veh. Syst. Dyn., vol. 44, no. sup1, pp. 560–570, 2006.

[21] H. Shi, G. Chen, and Y. Yang, “A comparative study on pantograph-catenary models and effect of parameters on pantograph-catenary dynamics under crosswind,” J. Wind Eng. Ind. Aerodyn., vol. 211, no. 104587, pp. 104587, 2021.

[22] M. Carnevale, A. Facchinetti, L. Maggiori, and D. Rocchi, “Computational fluid dynamics as a means of assessing the influence of aerodynamic forces on the mean contact force acting on a pantograph,” Proc. Inst. Mech. Eng. Pt. F: J. Rail Rapid Transit, vol. 230, no. 7, pp. 1698–1713, 2016.

[23] A. Othonos, “Fiber Bragg gratings,” Rev. Sci. Instrum., vol. 68, no. 12, pp. 4309–4341, 1997.

[24] K. O. Hill, Y. Fujii, D. C. Johnson, and B. S. Kawasaki, “Photosensitivity in optical fiber waveguides: Application to reflection filter fabrication,” Appl. Phys. Lett., vol. 32, no. 10, pp. 647–649, 1978.

[25] P. J. Lemaire, R. M. Atkins, V. Mizrahi, and W. A. Reed, “High pressure H2 loading as a technique for achieving ultrahigh UV photosensitivity and thermal sensitivity in GeO2 doped optical fibres,” Electron. Lett., vol. 29, no. 13, pp. 1191, 1993.

[26] G. Meltz, W. W. Morey, and W. H. Glenn, “Formation of Bragg gratings in optical fibers by a transverse holographic method,” Opt. Lett., vol. 14, no. 15, pp. 823–825, 1989.

[27] R. Kashyap, “Assessment of tuning the wavelength of chirped and unchirped fibre Bragg grating with single phase-masks,” Electron. Lett., vol. 34, no. 21, pp. 2025, 1998.

[28] M. Becker, T. Elsmann, I. Latka, M. Rothhardt, and H. Bartelt, “Chirped phase mask interferometer for fiber Bragg grating array inscription,” J. Lightwave Technol., vol. 33, no. 10, pp. 2093–2098, 2015.

[29] M. Becker, T. Elsmann, A. Schwuchow, M. Rothhardt, S. Dochow and H. Bartelt, "Fiber Bragg Gratings in the Visible Spectral Range With Ultraviolet Femtosecond Laser Inscription," in IEEE Photonics Technology Letters, vol. 26, no. 16, pp. 1653-1656, 15 Aug.15, 2014.

[30] M. Gagné, L. Bojor, R. Maciejko, and R. Kashyap, “Novel custom fiber Bragg grating fabrication technique based on push-pull phase shifting interferometry,” Opt. Express, vol. 16, no. 26, pp. 21550–21557, 2008.

[31] K. O. Hill, B. Malo, F. Bilodeau, D. C. Johnson, and J. Albert, “Bragg gratings fabricated in monomode photosensitive optical fiber by UV exposure through a phase mask,” Applied Physics Letters, vol. 62, no. 10, pp. 1035–1037, 1993.

[32] D. Z. Anderson, V. Mizrahi, T. Erdogan, and A. E. White, “Production of in-fibre gratings using a diffractive optical element,” Electron. Lett., vol. 29, no. 6, p. 566, 1993.

[33] R. Kashyap, A. Swanton, and D. J. Armes, “Simple technique for apodising chirped and unchirped fibre Bragg gratings,” Electron. Lett., vol. 32, no. 13, p. 1226, 1996.

[34] M. J. Cole, R. I. Laming, S. Barcelos, W. H. Loh, and M. N. Zervas, “Moving fibre/phase mask-scanning beam technique for enhanced flexibility in producing fibre gratings with uniform phase mask,” Electron. Lett., vol. 31, no. 17, pp. 1488–1490, 1995.

[35] L. M. Pereira et al., "Phase-Shifted Bragg Grating Inscription in PMMA Microstructured POF Using 248-nm UV Radiation," in Journal of Lightwave Technology, vol. 35, no. 23, pp. 5176-5184, 1 Dec.1, 2017.

[36] X. Hu, C.-F. J. Pun, H.-Y. Tam, P. Mégret, and C. Caucheteur, “Tilted Bragg gratings in step-index polymer optical fiber,” Opt. Lett., vol. 39, no. 24, pp. 6835–6838, 2014.

[37] C. A. F. Marques et al., “Chirped polymer optical fiber Bragg grating sensors,” in Micro-structured and Specialty Optical Fibres V, 2017.

[38] A. Halstuch and A. A. Ishaaya, “Femtosecond inscription of chirped fiber Bragg gratings and fiber Bragg grating arrays using a single uniform phase-mask,” Optics and Lasers in Engineering, vol. 160, p. 107286, 2023.

[39] N. Abdukerim, C. Hnatovsky, D. Grobnic, and S. Mihailov, “Femtosecond writing of tilted fiber Bragg gratings through the coating with a phase mask,” in 2019 Photonics North (PN), 2019.

[40] J. He et al., “Highly birefringent phase-shifted fiber Bragg gratings inscribed with femtosecond laser,” Opt. Lett., vol. 40, no. 9, pp. 2008–2011, 2015.

[41] S. M. Eaton, G. Cerullo, and R. Osellame, “Fundamentals of femtosecond laser modification of bulk dielectrics,” in Topics in Applied Physics, Berlin, Heidelberg: Springer Berlin Heidelberg, pp. 3–18, 2012.

[42] C. B. Schaffer, A. Brodeur, and E. Mazur, “Laser-induced breakdown and damage in bulk transparent materials induced by tightly focused femtosecond laser pulses,” Meas. Sci. Technol., vol. 12, no. 11, pp. 1784–1794, 2001.

[43] L.V. Keldysh. “Ionization in the Field of a Strong Electromagnetic Wave.” JETP, vol.20, pp.1307, 1965.

[44] R. Osellame, H. J. W. M. Hoekstra, G. Cerullo, and M. Pollnau, “Femtosecond laser microstructuring: an enabling tool for optofluidic lab-on-chips,” Laser Photon. Rev., vol. 5, no. 3, pp. 442–463, 2011.

[45] Y. Shimotsuma, P. G. Kazansky, J. Qiu, and K. Hirao, “Self-organized nanogratings in glass irradiated by ultrashort light pulses,” Phys. Rev. Lett., vol. 91, no. 24, p. 247405, 2003.

[46] S. Juodkazis et al., “Laser-induced microexplosion confined in the bulk of a sapphire crystal: evidence of multimegabar pressures,” Phys. Rev. Lett., vol. 96, no. 16, p. 166101, 2006.

[47] J. He, B. Xu, X. Xu, C. Liao, and Y. Wang, “Review of femtosecond-laser-inscribed fiber Bragg gratings: Fabrication technologies and sensing applications,” Photonic Sens., vol. 11, no. 2, pp. 203–226, 2021.

[48] A. Martinez, M. Dubov, I. Khrushchev, and I. Bennion, “Direct writing of fibre Bragg gratings by femtosecond laser,” Electron. Lett., vol. 40, no. 19, p. 1170, 2004.

[49] A. Martinez, I. Y. Khrushchev, and I. Bennion, “Direct inscription of Bragg gratings in coated fibers by an infrared femtosecond laser,” Opt. Lett., vol. 31, no. 11, pp. 1603–1605, 2006.

[50] G. D. Marshall, R. J. Williams, N. Jovanovic, M. J. Steel, and M. J. Withford, “Point-by-point written fiber-Bragg gratings and their application in complex grating designs,” Opt. Express, vol. 18, no. 19, pp. 19844–19859, 2010.

[51] R. J. Williams, N. Jovanovic, G. D. Marshall, and M. J. Withford, “All-optical, actively Q-switched fiber laser,” Opt. Express, vol. 18, no. 8, pp. 7714–7723, 2010.

[52] M. I. Skvortsov, A. A. Wolf, A. V. Dostovalov, A. A. Vlasov, V. A. Akulov, and S. A. Babin, “Distributed feedback fiber laser based on a fiber Bragg grating inscribed using the femtosecond point-by-point technique,” Laser Physics Letters, vol. 15, no. 3, p. 035103, 2018.

[53] Y. Wang et al., "Parallel-Integrated Fiber Bragg Gratings Inscribed by Femtosecond Laser Point-by-Point Technology," in Journal of Lightwave Technology, vol. 37, no. 10, pp. 2185-2193, 15 May15, 2019.

[54] F. Chen, X. Li, R. Wang and X. Qiao, "Multiple Cladding Fiber Bragg Gratings Inscribed By Femtosecond Laser Point-by-Point Technology," in Journal of Lightwave Technology, vol. 39, no. 23, pp. 7539-7544, Dec.1, 2021.

[55] Y. Sun, Y. Yao, H. Niu, H. Zha, L. Zhang, Z. Tian, N.-K. Chen, and Y. Ren, “Peak wavelength and bandwidth tunable fiber Bragg grating notch filter induced by femtosecond laser point by point inscription,” Optics Communications, vol. 521, pp. 128583, 2022.

[56] M. Wang et al., “Femtosecond laser fabrication of nanograting-based distributed fiber sensors for extreme environmental applications,” Int. J. Extrem. Manuf., vol. 3, no. 2, pp. 025401, 2021.

[57] M. L. Aslund et al., “Optical loss mechanisms in femtosecond laser-written point-by-point fibre Bragg gratings,” Opt. Express, vol. 16, no. 18, pp. 14248–14254, 2008.

[58] R. J. Williams, N. Jovanovic, G. D. Marshall, G. N. Smith, M. J. Steel, and M. J. Withford, “Optimizing the net reflectivity of point-by-point fiber Bragg gratings: the role of scattering loss,” Opt. Express, vol. 20, no. 12, pp. 13451–13456, 2012.

[59] K. Zhou, M. Dubov, C. Mou, L. Zhang, V. K. Mezentsev and I. Bennion, "Line-by-Line Fiber Bragg Grating Made by Femtosecond Laser," in IEEE Photonics Technology Letters, vol. 22, no. 16, pp. 1190-1192, Aug.15, 2010.

[60] B. Huang and X. Shu, "Line-by-Line Inscription of Phase-Shifted Fiber Bragg Gratings with Femtosecond Laser," in Asia Communications and Photonics Conference 2015, 2015.

[61] X. Xu et al., “Sapphire fiber Bragg gratings inscribed with a femtosecond laser line-by-line scanning technique,” Opt. Lett., vol. 43, no. 19, p. 4562, 2018.

[62] T. A. Goebel et al., “Realization of aperiodic fiber Bragg gratings with ultrashort laser pulses and the line-by-line technique,” Opt. Lett., vol. 43, no. 15, pp. 3794–3797, 2018.

[63] A. S. Chernikov, K. S. Khorkov, D. A. Kochuev, R. V. Chkalov, V. G. Prokoshev, and N. N. Davydov, “Line-by-line fiber Bragg grating fabrication by femtosecond laser radiation,” J. Phys. Conf. Ser., vol. 1164, pp. 012015, 2019.

[64] T. Erdogan, "Fiber grating spectra," in Journal of Lightwave Technology, vol. 15, no. 8, pp. 1277-1294, Aug. 1997.

[65] Y. Zhang, D. Qiao, Y. Zhu, and P. Jiang, “High-order fiber Bragg grating fabricated by femtosecond laser pulses for high-sensitivity temperature and strain sensing,” Optik (Stuttg.), vol. 222, no. 165423, pp. 165423, 2020.

[66] W.P. Huang, "Coupled-mode theory for optical waveguides: an overview," J. Opt. Soc. Am. A 11, vol. 11, pp. 963-983, 1994

[67] J. R. Pierce, "Coupling of modes of propagation", J. Appl.Phys., vol. 25, pp. 179-183, 1954.

[68] S. E. Miller, "On solutions of two waves with periodic coupling", Bell Syst. Tech. J., vol. 48, pp. 1801-1822, 1968.

[69] S. E. Miller, "Some theory and applications of periodically coupled waves", Bell Syst. Tech. J., vol. 49, pp. 2189-2218, 1969.

[70] C. C. H. Tang, "Mode conversion in nonuniform multimode waveguides and transitions" in Advances in Microwaves, vol. 4, pp. 301-372, 1969.

[71] H. C. Huang, "Coupled modes and nonideal waveguides" in Microwave Research Institute (MRI), NY:Polytechnique Inst. of Brooklyn, Nov. 1981.

[72] D. Marcuse, "The coupling of degenerate modes in two parallel dielectric waveguides", Bell Syst. Tech. J., vol. 50, pp. 1791-1816, 1971.

[73] H. Stoll and A. Yariv, “Coupled-mode analysis of periodic dielectric waveguides,” Opt. Commun., vol. 8, no. 1, pp. 5–8, 1973.

[74] H. A. Haus and W. Huang, "Coupled-mode theory," in Proceedings of the IEEE, vol. 79, no. 10, pp. 1505-1518, Oct. 1991.

[75] H. Kogelnik, “Theory of optical waveguides,” in Guided-Wave Optoelectronics, T. Tamir, Ed. New York: Springer-Verlag, pp. 7-88,1990.

[76] R. Kashyap, “Theory of fiber Bragg gratings,” in Fiber Bragg Gratings, R. Kashyap, Ed. San Diego, CA: Elsevier, pp. 119–187, 2010.

[77] K. Thyagarajan, “Optical fiber gratings,” in Guided Wave Optical Components and Devices, B. P. Pal, Ed. San Diego, CA: Elsevier, pp. 233–242, 2006.

[78] A. D. Kersey et al., "Fiber grating sensors," in Journal of Lightwave Technology, vol. 15, no. 8, pp. 1442-1463, Aug. 1997.

[79] W. W. Morey, G. Meltz, and W. H. Glenn, “Fiber optic Bragg grating sensors,” in Fiber Optic and Laser Sensors VII, 1990.

[80] S. Xu, F. Xing, R. Wang, W. Li, Y. Wang, and X. Wang, “Vibration sensor for the health monitoring of the large rotating machinery: Review and outlook,” Sensor Rev., vol. 38, no. 1, pp. 44–64, Jan. 2018.

[81] C.-Y. Hong, Y.-F. Zhang, M.-X. Zhang, L. M. Leung, and L.-Q. Liu, “Application of FBG sensors for Geotechniqueal Health Monitoring, a review of sensor design, implementation methods and packaging techniques,” Sensors and Actuators A: Physical, vol. 244, pp. 184–197, 2016.

[82] T. Li, J. Guo, Y. Tan and Z. Zhou, "Recent Advances and Tendency in Fiber Bragg Grating-Based Vibration Sensor: A Review," in IEEE Sensors Journal, vol. 20, no. 20, pp. 12074-12087, 15 Oct.15, 2020.

[83] C. K. Y. Leung et al., “Review: optical fiber sensors for civil engineering applications,” Mater. Struct., vol. 48, no. 4, pp. 871–906, 2015.

[84] Z. M. Hafizi and E. Vorathin, “Investigation of low frequency fibre Bragg grating accelerometer based on thermoplastic cantilever beam,” IOP Conference Series: Materials Science and Engineering, vol. 1078, no. 1, p. 012012, 2021.

[85] C. Z. Shi, “Cantilever optical vibrometer using fiber Bragg grating,” Opt. Eng., vol. 42, no. 11, p. 3179, 2003.

[86] Q. Liu, Z. Jia, H. Fu, D. Yu, H. Gao and X. Qiao, "Double Cantilever Beams Accelerometer Using Short Fiber Bragg Grating for Eliminating Chirp," in IEEE Sensors Journal, vol. 16, no. 17, pp. 6611-6616, Sept.1, 2016.

[87] L. Fang, T. Chen, R. Li and S. Liu, "Application of Embedded Fiber Bragg Grating (FBG) Sensors in Monitoring Health to 3D Printing Structures," in IEEE Sensors Journal, vol. 16, no. 17, pp. 6604-6610, Sept.1, 2016.

[88] D. Feng et al., "A Fiber Bragg Grating Accelerometer Based on a Hybridization of Cantilever Beam," in IEEE Sensors Journal, vol. 15, no. 3, pp. 1532-1537, March 2015.

[89] J. Cui, Z. Liu, D. S. Gunawardena, Z. Zhao, and H.-Y. Tam, “Two-dimensional vector accelerometer based on Bragg gratings inscribed in a multi-core fiber,” Opt. Express, vol. 27, no. 15, pp. 20848–20856, 2019.

[90] F. Chen, X. Li, R. Wang, and X. Qiao, “Two-dimensional vector accelerometer based on orthogonal Bragg gratings inscribed in a standard single-mode fiber cladding,” Opt. Lett., vol. 46, no. 12, pp. 2992–2995, 2021.

[91] Q. Rong, X. Qiao, T. Guo, W. Bao, D. Su, and H. Yang, “Orientation-dependent fiber-optic accelerometer based on grating inscription over fiber cladding,” Opt. Lett., vol. 39, no. 23, pp. 6616–6619, 2014.

[92] F. Chen, R. Wang, X. Li, and X. Qiao, “Orientation-dependent fiber-optic accelerometer based on eccentric fiber Bragg grating,” Opt. Express, vol. 29, no. 18, pp. 28574–28581, 2021.

[93] F. Chen, D. Su, X. Qiao and Q. Rong, "Compact Vector Bend Sensor Using Dual-Off-Axis Innermost Cladding-Type FBGs," in IEEE Sensors Journal, vol. 18, no. 18, pp. 7476-7480, 15 Sept.15, 2018.

[94] W. Bao, X. Qiao and Q. Rong, "Fiber-Optic Vector Accelerometer Using Orthogonal Bragg Grating Inscription Over Innermost Cladding of a Multi-Clad Fiber," in Journal of Lightwave Technology, vol. 37, no. 11, pp. 2706-2712, 1 June1, 2019.

[95] Y. Zhang et al., "2-D Medium–High Frequency Fiber Bragg Gratings Accelerometer," in IEEE Sensors Journal, vol. 17, no. 3, pp. 614-618, 1 Feb.1, 2017.

[96] L. Wei, L. Yu, J. Wang, D. Jiang, Q. Liu and Z. Liu, "An FBG-Sensing Two-Dimensional Vibration Sensor Based on Multi-Axis Flexure Hinge," in IEEE Sensors Journal, vol. 19, no. 10, pp. 3698-3710, 15 May15, 2019.

[97] H. Wang, B. Yan and L. Liang, "A 3D FBG Accelerometer Based on Two Pairs of Flexible Hinges," in IEEE Sensors Journal, vol. 21, no. 19, pp. 21586-21593, 1 Oct.1, 2021.

[98] A. Fender et al., "Two-Axis Temperature-Insensitive Accelerometer Based on Multicore Fiber Bragg Gratings," in IEEE Sensors Journal, vol. 8, no. 7, pp. 1292-1298, July 2008.

[99] H. Wu, Q. Lin, F. Han, L. Zhao, and Z. Jiang, “Design and analysis of high-frequency fiber Bragg grating vibration sensor,” Measurement Science and Technology, vol. 32, no. 2, pp. 025108, 2020.

[100] P. Zdziebko, P. Kurowski, A. Martowicz, and T. Uhl, “Load cell for active pantograph solution based on the Fiber-Bragg grating sensor,” 2018.

[101] B. J. Goodno and J. M. Gere, Mechanics of Materials, 9th ed. Australia: Cengage Learning, 2018.

[102] N. Basumallick, I. Chatterjee, P. Biswas, K. Dasgupta, and S. Bandyopadhyay, “Fiber Bragg grating accelerometer with enhanced sensitivity,” Sens. Actuators A Phys., vol. 173, no. 1, pp. 108–115, 2012.

[103] S. Bruni et al., “The results of the pantograph–catenary interaction benchmark,” Veh. Syst. Dyn., vol. 53, no. 3, pp. 412–435, 2015.

[104] EN50317:2012. Railway applications Current collection systems Requirements for and validation of measurements of the dynamic interaction between pantograph and overhead contact line. CENELEC, 2012.

[105] S. C. Ryu and P. E. Dupont, "FBG-based shape sensing tubes for continuum robots," 2014 IEEE International Conference on Robotics and Automation (ICRA), Hong Kong, China, pp. 3531-3537, 2014.

[106] M. Abayazid, M. Kemp and S. Misra, "3D flexible needle steering in soft-tissue phantoms using Fiber Bragg Grating sensors," 2013 IEEE International

Conference on Robotics and Automation, Karlsruhe, Germany, pp. 5843-5849, 2013.